GLIA

WILEY

RESEARCH ARTICLE

Integrity of neural extracellular matrix is required for microglia-mediated synaptic remodeling

Carla Cangalaya[1] | Weilun Sun[1,2] | Stoyan Stoyanov[1] | Ildiko Rita Dunay[3,4] 🔟 | Alexander Dityatev[1,4,5] 🔟

[1]Molecular Neuroplasticity Group, German Center for Neurodegenerative Diseases (DZNE), Magdeburg, Germany

[2]Department of Pharmacology, School of Pharmaceutical Sciences, Jilin University, Changchun, China

[3]Institute of Inflammation and Neurodegeneration, Otto von Guericke University Magdeburg, Magdeburg, Germany

[4]Center for Behavioral Brain Sciences (CBBS), Magdeburg, Germany

[5]Medical Faculty, Otto von Guericke University, Magdeburg, Germany

Correspondence
Alexander Dityatev, Molecular Neuroplasticity Group, German Center for Neurodegenerative Diseases (DZNE), Leipziger Str. 44, Haus 64, 39120 Magdeburg, Germany.
Email: alexander.dityatev@dzne.de

Abstract

Microglia continuously remodel synapses, which are embedded in the extracellular matrix (ECM). However, the mechanisms, which govern this process remain elusive. To investigate the influence of the neural ECM in synaptic remodeling by microglia, we disrupted ECM integrity by injection of chondroitinase ABC (ChABC) into the retrosplenial cortex of healthy adult mice. Using in vivo two-photon microscopy we found that ChABC treatment increased microglial branching complexity and ECM phagocytic capacity and decreased spine elimination rate under basal conditions. Moreover, ECM attenuation largely prevented synaptic remodeling following synaptic stress induced by photodamage of single synaptic elements. These changes were associated with less stable and smaller microglial contacts at the synaptic damage sites, diminished deposition of calreticulin and complement proteins C1q and C3 at synapses and impaired expression of microglial CR3 receptor. Thus, our findings provide novel insights into the function of the neural ECM in deposition of complement proteins and synaptic remodeling by microglia.

KEYWORDS
C1q, C3, complement protein, extracellular matrix, microglia, spine, synapse, two-photon microscopy

1 | INTRODUCTION

The neural extracellular matrix (ECM) is an essential component of inhibitory and excitatory synapses and, together with glial and synaptic terminals, forms the "tetrapartite synapse" (Dityatev et al., 2006; Dityatev & Rusakov, 2011; Dityatev & Schachner, 2006; Faissner et al., 2010). The ECM provides a scaffold for synaptic structures, which is essential for their stabilization and shaping, and regulates synaptic plasticity (Dityatev et al., 2010; Dityatev & Schachner, 2003; Lively & Schlichter, 2013; Senkov et al., 2014). Previously, it has been shown that ECM degradation causes marked instability in dendritic spines and promotes synaptic plasticity (De Vivo et al., 2013; Orlando et al., 2012).

On the other hand, microglia constantly monitor and sculpt synapses to maintain efficient neural communication (Helmut et al., 2011; Nimmerjahn et al., 2005; Wake et al., 2009). The intricate connection between synapses and the ECM in which they reside suggests that changes in the ECM may affect their function, and their interaction with microglia. However, the precise role of the ECM in the functional interaction between microglia and synapses remains elusive. Microglial cells may modulate both condensed (perineuronal nets or PNNs) and diffuse (perisynaptic) forms of neural ECM (Deepa et al., 2006; Dityatev et al., 2010; Fawcett et al., 2019; Galtrey et al., 2007; Hockfield et al., 1990; Schwartz & Domowicz, 2018). This is supported by the observations that chronic depletion of microglia leads to an accumulation of PNNs (Crapser, Spangenberg, et al., 2020a) and perisynaptic ECM containing brevican in the healthy mouse brain (Strackeljan et al., 2021). Furthermore, it has recently been shown that adult microglia degrade perisynaptic ECM proteins (aggrecan and brevican) to promote memory consolidation in response to neuronal IL-33 release (Nguyen et al., 2020). Research in the field of neuroinflammation provided further evidence of the bidirectional interaction between the ECM and microglia. For example, microglia-mediated PNN loss has been observed in systemic inflammation (Crapser, Spangenberg, et al., 2020a), Alzheimer's disease, Huntington's disease (Crapser, Ochaba, et al., 2020), and schizophrenia (Berretta et al., 2015; Kaushik et al., 2021; Matuszko et al., 2017; Venturino et al., 2021). Our previous work suggests that ECM controls microglial behavior in the early stages of amyloidosis (Stoyanov et al., 2021). In this study, the application of Chondroitinase ABC (ChABC)—which targets the ECM by mainly degrading chondroitin and dermatan sulfates side chains but also hyaluronan—ameliorated the altered migration of microglialc cells in the cortex of 5xFAD mice. Based on these and other observations (Kettenmann et al., 2013; Milner & Campbell, 2003), it is plausible to assume that the neural ECM may regulate microglial functions.

Here, we directly investigated the role of the neuronal ECM in synaptic remodeling by microglia using two-photon vital microscopy. The retrosplenial cortex (RSC) was chosen for imaging due to the high levels of ECM expression (Lupori et al., 2023; Stoyanov et al., 2021) and its key role in spatial navigation, memory, and history-dependent value coding (Hattori et al., 2019).

In vivo imaging in the RSC and targeted laser photoablation (Cangalaya et al., 2020) demonstrated that ECM degradation mitigates spine loss, microglial contact with spines, and complement protein deposition. These findings highlight the ECM as a potential therapeutic target for modulating microglia-mediated synaptic remodeling, which is severely unbalanced in favor of synaptic loss in neurodegenerative diseases including Alzheimer's disease.

2 | METHODS

2.1 | Ethics statement

All animal handling followed the ethical guidelines of Directive 2010/63/EU, German law, and Saxony-Anhalt state's Ethical Committee on Animal Health and Care (license number: 42502-2-1346).

2.2 | Animals

We generated triple transgenic Cx3cr1$^{Cre/Tomato}$ × GFPM Thy-1 mice with a C57BL6J background using Cre/lox system to achieve cell-type-specific fluorescence expression (Madisen et al., 2010). For this, we crossbred mice expressing enhanced green fluorescent protein (EGFP) under the control of a modified Thy-1 promoter region (Feng et al., 2000) (GFPM Thy-1 # 007788 from The Jackson Laboratory) with mice expressing red fluorescent protein dtTomato in microglia driven by the endogenous Cx3cr1 locus (Yona et al., 2013) (Cx3cr1$^{Cre/Tomato}$ obtained by crossbreeding of # 007905 and # 020940 lines from The Jackson Laboratory). The mice were housed at 22°C with 65% humidity under a 12-h light/dark cycle. The mice received food and water ad libitum.

In this exploratory study, to maximize our chance of detecting microglial effects, we chose male mice. Microglia are known to exhibit sex-dependent responses, with males displaying higher motility (Lenz & McCarthy, 2015; Villa et al., 2018) and greater susceptibility to inflammatory activation compared to females (Villa et al., 2018).

2.3 | Tamoxifen intraperitoneal administration for induction of CreERT2 activity

Before injection, a fresh solution of tamoxifen powder (T5648, Sigma) was prepared by dissolving it in corn oil (20 mg/mL). The solution was then shaken at room temperature overnight and protected from light. P30–P45 mice received daily intraperitoneal injections of 2 mg tamoxifen (delivered in a 100 μL volume) for 5 days to induce CreERT2-mediated recombination (Madisen et al., 2010).

2.4 | Stereotaxic injection of ChABC

Intracerebral bilateral injections (one per hemisphere) of 200 nL of either 50 U/mL ChABC (AMS.E 1028-10, AMSIBIO, Europe) in phosphate-buffered saline (PBS) with 0.1% bovine serum albumin

(BSA) or vehicle (PBS with 0.1% BSA) were performed into the RSC at the following coordinates: AP: −2.0 mm; ML: 0.5 mm; DV: 0.5 mm with a 10 µL NanoFil syringe (World Precision Instruments, USA) using an Ultra Micro Pump (UMP3, World Precision Instruments, USA) at a speed of 100 nL/min (500 nL per site) under isoflurane anesthesia (Stoyanov et al., 2021). After each injection, the needle was left in position for 5 min before being gradually removed. These injections were performed after the removal of the drilled skull piece and before the glass coverslip placement.

2.5 | Surgery procedures (cranial window preparations)

Mice were anesthetized using isoflurane within a specialized chamber (Baxter, Germany). Anesthetized mice were positioned in a stereotaxic apparatus (SR-6M, Narishige Scientific Instrument Lab, Japan) to ensure precise head immobilization. An electric heating pad (ATC1000, World Precision Instruments, USA) maintained the body of the mouse at 37°C for optimal physiological function. Eye lubricant was applied to prevent corneal dryness and discomfort. All surgical instruments and the surrounding area were sterilized to ensure aseptic conditions and minimize infection risk. Isoflurane levels were adjusted to maintain anesthesia at 1.5%–2%. Oxygen levels were set to 0.4 L/min using an isoflurane vaporizer (Matrix VIP 3000, Midmark, USA). An incision was made on the scalp to remove fur and skin, and soft tissues were gently retracted for clear access to the skull. Utilizing a surgical stereoscope and a high-speed dental drill, a circular craniotomy was performed at a precise location: 2 mm anterior and 2 mm lateral to bregma. Bone fragments were carefully removed and bleeding was controlled with sterile cotton applicators and saline solution (NaCl). The exposed brain surface and the outer edges of the craniotomy were dried and gently rinsed with PBS. A circular glass coverslip (5 mm diameter, Thermo Scientific) was placed directly above the brain tissue and sealed with cyanoacrylate glue (Pattex-Henkel, Germany) applied onto the outermost layer of the brain, the dura mater. Dental cement (Paladur, Heraeus Kulzer, Germany) was then applied to further secure the glass coverslip, protect the brain tissue, and provide a watertight seal around the implanted window. Finally, a rectangular head plate was positioned over the glass coverslip and secured with additional cyanoacrylate glue (Pattex-Henkel, Germany). The glue was allowed to be set for approximately 5–10 min. Following surgery, mice were transferred to a dedicated recovery cage with a warm environment to facilitate recovery. Postsurgical pain relief was provided by administering the analgesic ketoprofen (5 mg/kg body weight) for 3 days.

2.6 | Two-photon microscopy

Fluorescent signals in the RSC of mice were visualized using two-photon microscopy (2PM), employing a Ti:Sapphire laser (Chameleon Vision II, Coherent) for high-energy, pulsed light necessary for two-photon excitation. This light was then detected by a multiphoton microscope (LSM 7 MP, Carl Zeiss, Germany), and a 20× water immersion objective lens (Zeiss, N.A. = 1.0) to focus the laser light onto the brain tissue and collect the emitted fluorescence. The fluorescence signals of EGFP (green fluorescence) and tdTomato (red fluorescence) were excited at 900, 1040, and 600 nm wavelengths, respectively. Prior to imaging, mice were anesthetized with an intraperitoneal injection of ketamine (90 mg/kg body weight) and xylazine (18 mg/kg of body weight) in 0.9% NaCl solution, body temperature was maintained at 37°C using a heating pad, and eyes were shielded with eye ointment (Bepanthen) to prevent dehydration. To prevent photodamage, the pixel dwell time was maintained between 1 and 2.5 ms and images were acquired using a low laser power (less than 30 mW at the sample). Stacks of images were acquired using a 20× water immersion objective in layers 2/3 of the dysgranular RSC of each animal, at depths between 120 and 180 µm (layer 5 starts at 300 µm) to visualize Thy-1-EGFP-positive excitatory neurons and their neighboring microglial cells.

2.7 | Synaptic photodamage

In this study, we used laser photodamage to target dendritic spines and boutons. We applied laser photodamage directly to the spine (Spine-PD), 1 µm above the spine head (Near-Spine-PD), and 1 µm above the axonal bouton (Near-Bouton-PD) using a laser beam focused into a line approximately 1 µm length, with a power ranging from 150 to 200 mW at the sample and an excitation wavelength of 850 nm (60 cycles, and a total irradiation duration of 1 s).

To assess the success of our experiments, we measured the lifetime of each targeted spine. A successful Spine-PD experiment required the spine to disappear within the first 30 min of recording. For Near-Spine-PD experiments, the spine needed to remain stable for the first 30 min. For a successful Near-Bouton-PD experiment, the targeted bouton needed to have a lifetime of more than 30 min.

We took special care to prevent transient swelling by introducing photodamage far from the dendritic branch and axonal shaft. Before selecting spines/boutons for ablation, we selected dendritic and axonal branches with similar density and thickness. We specifically chose tertiary and secondary branches with a thickness of no more than 2 µm and a high percentage of spines in one optical plane (Holmes and Berkowitz, 2014). For axonal branches, we selected ones with en passant boutons (EPBs) with areas of 1–2 µm^2 and no terminal boutons. We imaged dendritic segments with a mean ± SD length of 27 ± 3.5 µm or axonal segments of 38 ± 4.6 µm.

Within these branches, we chose spines/boutons for photodamage based on the following criteria: Well-defined structures that are not contacted by microglia, and have no closely located neighboring spines/boutons. Due to the clustering of spines in the cortex (Gökçe, eLife 2016), we verified whether the structures selected for photodamage were not within spine clusters. For this, we compared the average distance between the targeted structure and its closest neighbors to the average distance between all neighboring spines/boutons

per dendritic/axonal segment. Spines targeted for photodamage were not within clusters and displayed slightly greater distances from their closest neighbors compared to the average interspine distance in the selected dendrites.

All three laser-photodamage types were performed in triplicate in three different fields of view. These fields of view were separated by more than 250 μm to ensure data collection from distinct neurons. However, in the case of axonal branches, we cannot rule out that they originated from the same neuron due to the extensive axon collateralization in the cortex. We identified these fields of view at low magnification (20× objective, zoom factor: 1.5; 1024 × 1024 pixels; image size 292.01 μm × 292.01 μm; a z-stack of 20 optical sections with 2 μm z-spacing). We used the brain vasculature as a reference point to ensure we were imaging the same areas longitudinally.

Before photodamage, we acquired a z-stack to obtain a 3D reconstruction of the dendrite or axonal branch. We used a 20× objective with a zoom factor 5, 1024 × 1024 pixels, image size 85.02 μm × 85.02 μm, and a z-stack of 5–9 optical sections with 1 μm z-spacing. We followed up with imaging every 10 min for 2 h, both before and after photodamage.

2.8 | 2PM image processing

For each mouse, we successfully collected two to three replicates per photodamage type, along with corresponding baseline images before and after photodamage. Each recording lasted 2 h, capturing images every 10 min. The resulting image stacks consisted of 5–10 z-slices, 13 time points, and 2 channels (EGFP and tdTomato). For image processing and parameter analysis, we selected a 50 μm × 50 μm region of interest (ROI) within each image stack. Within each ROI stack, images were aligned using the dendritic branch as a reference point. Alignment was performed using the Linear Stack Alignment with Sift and MultiStackReg plugins within the Fiji software (Thévenaz et al., 1998).

Microglia–neuron area contact: Microglia contact area with dendrites or axons was quantified as the colocalization of EGFP (microglia) and tdTomato (dendrite/axon) channels at each time point (13 in total). This colocalization area was calculated in μm^2 using a custom Fiji macro that automated the process. First, a dendrite/axon was isolated: Neighboring dendrites and axons were manually removed from the EGFP channel to focus on a single branch. Second, a maximum intensity projection was generated from the original Z-stacks to obtain a single image representing the entire structure. Third, the contact area was calculated. The colocalization area (μm^2) between EGFP and tdTomato channels was measured using the Coloc2 plugin within Fiji. Fourth, normalization of the contact area was performed. To account for differences in dendrite/axon size, the colocalization area (μm^2) was divided by the total area of the studied dendrite/axon segment (EGFP-positive area) and multiplied by 100 for each time point. Finally, the average contact area was calculated: the "Microglia-Neuron contact area %" was set to the average of the normalized contact area across all 13 time points.

Microglia-contacted spines and boutons percentage and duration: To determine the percentage of microglia-contacted spines or boutons, we performed a qualitative analysis. Microglia were considered to be in contact with a spine or bouton if more than 20% of its surface area overlapped with the microglia in at least one image slice of the z-stack and at least one time point during the imaging session. The "microglia-contacted spine or bouton percentage" was calculated by dividing the total number of contacted structures by the total number of observed structures and multiplying by 100. Additionally, we assessed the "microglia-contact duration" by measuring the total time (in min) that each individual spine or bouton remained in contact with microglia throughout the imaging session. For statistical analysis, all parameters were averaged for each mouse.

Spine turnover: Within each ROI, we focused on a specific dendritic segment approximately 30 μm in length. Using the original z-stacks and the 3D convolution viewer in ZEN software (Carl Zeiss), spines were manually counted without any prior knowledge of the baseline configuration. To quantify spine turnover, we identified and counted "lost" and "gained" spines based on previously established criteria (Holtmaat et al., 2005). Spines were considered "gained" if they had a length exceeding 0.4 μm (5 pixels), and "lost" if their length fell below this threshold. Spine length was estimated from the base at the dendritic shaft to the tip of the spine head. Additionally, spines were classified as "lost" if their position on the dendrite shifted by ≥0.5 μm relative to neighboring spines. The "turnover percentage" (%) was then calculated as the proportion of spines appearing or disappearing between consecutive time points. This was calculated by summing the number of gained and lost spines from the previous time point to the analyzed time point, dividing by the total number of spines at both time points, and multiplying by 100. Individual percentages of "gained" (formation of spines %) and "lost" spines (elimination of spines %) were also determined by dividing the number of gained or lost spines by the total number of spines at each time point and multiplying by 100. Furthermore, the "mean turnover rate (%)" was calculated by averaging the individual turnover rates (%) across all 13 time points. Similarly, mean percentages of gained and lost spines were obtained by averaging the individual percentages at each time point across the 13 time points.

Axonal bouton turnover: For this study, we selected axonal segments approximately 40 μm long that clearly displayed EPBs. These EPBs were required to have a specific area range (1–2 μm^2) and lack terminal boutons. To identify newly formed ("gained") and disappearing ("lost") axonal boutons across the time points, we employed validated criteria established by Holtmaat et al. (2008). According to these criteria, a "gained" bouton had to be three times brighter than the surrounding axonal backbone. Conversely, a bouton was considered "lost" if its brightness decreased to less than 1.3 times the backbone brightness. However, to ensure we were not scoring transient structures like transport packets or moving organelles, we only considered EPBs that remained at the same site for at least two consecutive time points (10 min). Additionally, to distinguish between closely positioned boutons, they needed to be separated by at least 2 μm in at least one z-plane.

The "turnover percentage (%)" for axonal boutons was calculated using the same calculation as for spine turnover.

Filopodia detection and measurements: Spine head filopodia (SHF) were defined as protrusions extending from the spine head longer than 0.5 μm and with a thickness half or less than the spine head itself. For boutons, filopodia were identified as processes exceeding 1 μm in length and originating from EPBs (Wu et al., 2012). We characterized filopodia from both spines and boutons using three parameters: occurrence, size, and duration. Occurrence: We tracked the presence or absence of filopodia throughout the 2-h observation period. The total number of filopodia formation events was divided by the total number of spines or boutons tracked and multiplied by 100. Size: We measured the filopodium length from the spine head to the tip of the SHF. The longest observed length during the 2 h served as the basis for statistical comparisons. Duration: We traced all filopodium events throughout the observation period and recorded their lifetime in min.

2.9 | Morphological microglia analysis

Z-stack images were captured with a 20× objective on a 2PM at 1.5 μm intervals of RSC. Image analysis was carried out using ImageJ. First, all z-stack images were transformed into z-projected images. Subsequently, a uniform threshold correction was applied to all images, followed by binarization and the application of unsharp mask and despeckle filters to eliminate noise. For microglia morphology analysis, the "magic" selection tool was utilized to outline the cell body projections to determine the number, soma area, and circularity of microglia. To assess branch number and length, images were skeletonized and analyzed using the AnalyzeSkeleton plugin in FIJI. Branches with ≤2 endpoints and <10 pixels in length were excluded. The total number of endpoints and the average branch length were computed for each image, then divided by the number of microglia somas in the ROI to obtain the overall microglia branch count and total microglial branch length, respectively (Fung et al., 2020; Morrison & Filosa, 2013; Tejera et al., 2019; Young & Morrison, 2018). A parallel analysis was conducted using confocal images (21-μm z-stack at 2-μm intervals, captured with a Zeiss 510, 40×/1.3 oil objective) in both ipsilateral and contralateral RSC.

2.10 | Confocal analysis

The mice were anesthetized with ketamine/xylazine; 90 mg/kg and 18 mg/kg body weight in 0.9% NaCl solution, and subjected to transcardial perfusion with PBS and 4% paraformaldehyde (PFA). Subsequently, the brains were fixed in 4% PFA for 48 h at 4°C and two changes of 30% sucrose solutions, and frozen in 100% 2-methylbutane (kept at −80°C) and stored at −80°C until sectioning for subsequent analysis. Coronal brain sections, 40 μm in thickness, were prepared using a cryostat (Leica CM1950, Germany). These freely floating sections were subsequently stored in a cryoprotectant solution (30% ethylene glycol, 30% glycerol, 10% 0.2 M sodium phosphate buffer pH 7.4, in dH2O). For immunofluorescence, brain sections were washed three times with PB (phosphate buffer, PH 7.4), permeabilized for 1 h with a blocking solution (0.1% Triton X-100, glycine 10%, normal goat serum, in PB buffer), and incubated with primary antibodies for 48 h (rabbit anti-Iba1, Wako, Cat. Number: 019–19741, dilution 1:500; guinea pig anti-Iba1, Synaptic Systems, Cat. Number: 234004, dilution 1:1000; guinea pig anti-Homer1, Synaptic system, Cat. Number: 160004, dilution 1:500; rat anti-CD68, R&D systems, Cat. Number: MCA1957, dilution 1:500; rat anti-C1q, abcam, Cat. Number: ab11861, dilution 1:1000; anti-rat C3, Hycultec, Cat. Number: HM1045, dilution 1:500; rabbit anti-calreticulin (CRT), Cell Signaling, Cat. Number:12238S, dilution 1:500; rat anti-C3R, Hycultec, Cat. Number: HM3028, dilution 1:500; biotinylated *Wisteria floribunda* agglutinin (WFA), Vector Laboratories, Cat. Number: B-1355, dilution 1:500; rabbit anti-Aggrecan, Millipore, Cat. Number: AB1031, dilution 1:500; guinea pig anti-brevican, dilution 1:500; sheep anti-Neurocan, R&D Systems, Cat. Number: AF5800, dilution 1:500; mouse anti-Tenascin-R, Santa-Cruz, Cat. Number: sc-9875) in constant agitation. After washing three times with PB, secondary antibodies (Alexa Fluor 647-conjugated secondary anti-rabbit antibody, Life Technologies-Invitrogen, Cat. Number: A-21245, dilution 1:250; Alexa Fluor 647-conjugated secondary anti-rat antibody, Jackson, Cat. Number: 712-605-153, dilution 1:250; Alexa Fluor 647-conjugated secondary anti-mouse antibody, Life Technologies-Invitrogen, Cat. Number: A-21235, dilution 1:250; Alexa Fluor 647-conjugated secondary goat anti-sheep antibody, ThermoFisher, Cat. Number: A-21448, dilution 1:250; Alexa Fluor 405-conjugated secondary anti-guinea pig antibody, Sigma Aldrich, Cat. Number: SAB4600467, dilution 1:250) were applied for 3 h. Confocal images were acquired with various objectives and z-stacks captured at 1 μm intervals. These images were then processed and displayed as maximum-intensity projections.

2.11 | Immunofluorescence quantification

Microglial engulfment quantification: For this analysis, we utilized z-stack images to blindly quantify microglial engulfment. First, a consistent threshold across all images within a stack was determined based on the histogram of the entire stack. This threshold was then applied to create a microglia mask. To enhance microglial features and separate them from background noise, an unsharp mask filter was employed. However, this filter can introduce salt-and-pepper noise. To address this, a subsequent despeckle step effectively eliminated these artifacts outside the regions of interest (Lian et al., 2016). Next, a custom ImageJ macro based on Otsu's method in the hue, saturation, value (HSV) color space and color thresholding was used to generate a profile of colocalization pixels between CD68 and Homer-1 or ECM proteins. Finally, for automated 3D colocalization pixel recognition and quantification per microglia cell within the z-stack images, we employed in parallel both the 3D object counter plugin of ImageJ (Bolte & Cordelières, 2006) and the 3D viewer in Zen software.

To quantify the expression of C1q, C3R, CRT, and C3 within microglia, we employed a two-step approach. First, we extracted microglia masks across z-stacks. Then, we utilized the 3D object counter plugin for ImageJ to quantify the mean intensity and area for each marker within microglia cells.

To assess C1q/CRT colocalization with spines, images were acquired using the same parameters as described for synaptic engulfment analysis to ensure consistency. We employed the SynapseCounter plugin in ImageJ (Dzyubenko et al., 2016) for consistent thresholding across all channels and to recognize colocalization puncta. Additionally, image smoothing (Nguyen et al., 2020) was applied to reduce noise. The colocalized areas were then overlaid with skeletonized images of the Thy-1 channel. This allowed us to determine the number of spines associated with C1q or CRT. To ensure accuracy, a manual inspection of z-stacks was performed for further confirmation. Quantification was carried out on secondary and tertiary dendritic branches oriented parallel to the optical plane (5–10 dendrites per mouse, average length = 78 μm, range = 39–134 μm).

2.12 | Statistics

R 4.3.2 version and RStudio 2023.09.1 + 494 software were used for data management and statistical analysis. The package ggplot2 of R was used to create graphs. Here, all graphs and statistics are shown per animal as a unit of observation (the data from replicates from the same animal were averaged separately for Spine-PD, Near-Spine-PD, and Near-Bouton-PD). For comparison of spine density (%), turnover (%), elimination of spines/boutons (%), formation of spines/boutons (%), filopodia occurrence (%), neuron–microglia contact area (%), number of microglia-contacted spines/boutons (%), duration of contact (min) between different groups or experiments, mixed ANOVA with repeated measures, and generalized estimating equations (GEE) (R packages: lmer4, geepack, and emmeans) were used. Besides, GEE and linear mixed model analysis were performed using an independent within-group correlation structure to calculate the interaction between time and treatment groups followed by Tukey's post hoc tests for pairwise comparisons (Model: time as repeated measures, treatment as a fixed factor, time as a covariate, and their interaction treatment × time). Data from ex vivo specimens were analyzed using an unpaired generalized linear model (GLM) with Tukey's post hoc tests for multiple comparisons. For all reported differences between groups, the *p*-values are <.05.

3 | RESULTS

### 3.1 | ChABC treatment degrades the neural ECM in the RSC

To study the role of ECM in modulating the interaction between microglia and synapses, we used ChABC to compromise the integrity of the ECM by digesting chondroitin sulfates (Brückner et al., 1998;

Deepa et al., 2006) and hyaluronan (Deepa et al., 2006; Galtrey et al., 2007; Lin et al., 2008). To visualize the interactions between microglia and neurons, the $Cx3cr1^{Cre/Tomato}$ × GFPM Thy-1 transgenic mouse line was utilized in which red (tdTomato) and green (EGFP) fluorescent proteins are selectively expressed in microglia and a subset of cortical glutamatergic neurons, respectively (Cangalaya et al., 2020). The RSC was selected for two-photon imaging as a brain region rich in ECM expression (Lupori et al., 2023; Stoyanov et al., 2021) and crucial in spatial orientation, memory, and contextual associations (Hattori et al., 2019). Ten male adult animals (3- to 4-month-old) were randomly allocated to two separate experimental groups of 5 mice each. One group received intracerebral injections of ChABC into the RSC and the other group received vehicle injections before the implantation of cranial windows (Figure 1a). Following the intracerebral administration of ChABC or vehicle, skull cranial windows were set over the RSC for all mice to achieve repetitive in vivo two-photon imaging of the same brain area 1 and 7 days after the surgery (Figure 1a).

Previous studies have demonstrated the effectiveness of ChABC injection in ECM digestion by removing chondroitin sulfate side chains at 1, 3, and 7 days postinjection (Hayani et al., 2018; Stoyanov et al., 2021). To evaluate the extent of ECM digestion in the RSC, we used WFA, which specifically recognizes some of chondroitin sulfate side chains targeted by ChABC and stains PNNs. WFA staining was strongly ablated in the ChABC-injected group compared to the control brains at day 1 (D1) (Figure S1) and day 7 postinjection (D7) (Vehicle: 11.28 ± 1.80 vs. ChABC: 0.62 ± 0.11, *p* = .001) (Figure 1b). Similarly, immunolabeling of chondroitin sulfate proteoglycans (CSPGs), such as aggrecan (Vehicle: 8.76 ± 1.64 vs. ChABC: 2.15 ± 0.57, *p* = .009), brevican (Vehicle: 7.47 ± 1.04 ChABC: 0.57 ± 0.18, *p* = .0006), and neurocan (Vehicle: 8.64 ± 0.75 vs. ChABC: 3.10 ± 0.39, *p* = .0006) showed a marked loss in their expression at D7 in the ChABC group, accompanied also by a decrease in expression of CSPG cross-linking glycoprotein tenascin-R (TN-R) (Vehicle: 7.76 ± 1.9 vs. ChABC: 0.96 ± 0.40 vs. *p* = .013) (Figure 1c,d). Interestingly, we found an increase in WFA-positive puncta inside microglial bodies in the ChABC group at D7 (Vehicle: 0.017 ± 0.005 vs. ChABC: 0.074 ± 0.015, *p* = .011), demonstrating microglial contribution to ECM degradation after ChABC treatment (Figure 1e).

3.2 | ChABC treatment modifies microglia morphology

Intracerebral injection of ChABC has been shown to modulate microglial recruitment (Didangelos et al., 2014; Stoyanov et al., 2021), and promote microglia polarization and release of anti-inflammatory cytokines (Didangelos et al., 2014). Here, ChABC attenuated microglia recruitment observed in the injection area in the control group 7 days after injection (512.98 ± 30.09 vs. 346.13 ± 40.80 cells per mm^2, *p* = 0.044) (Figure 2a,b). Next, we tested whether the morphological state of microglia was modified after ChABC treatment using semiautomated analysis of microglia soma and branching processes. No differences in total microglia area were found between treatments
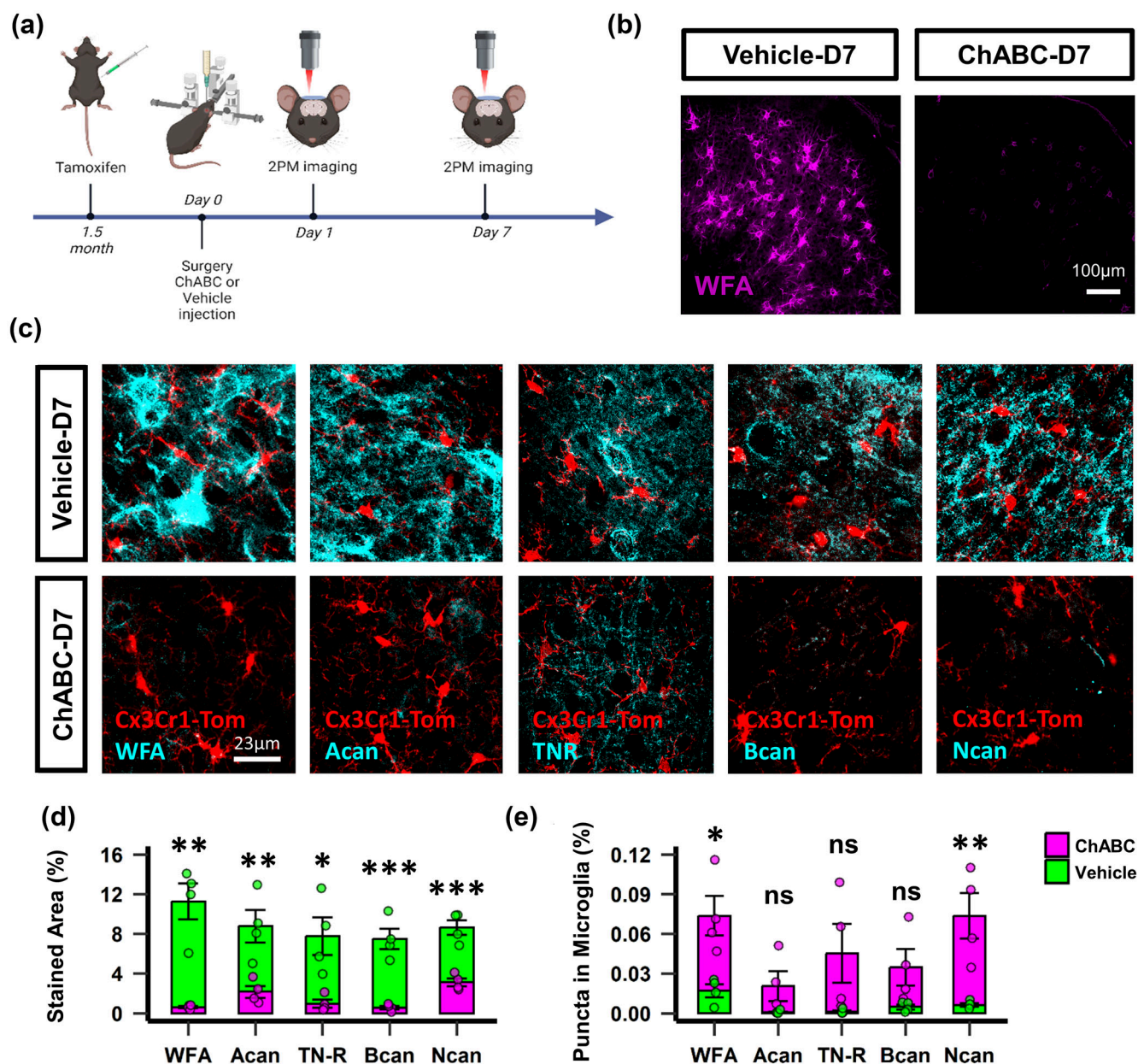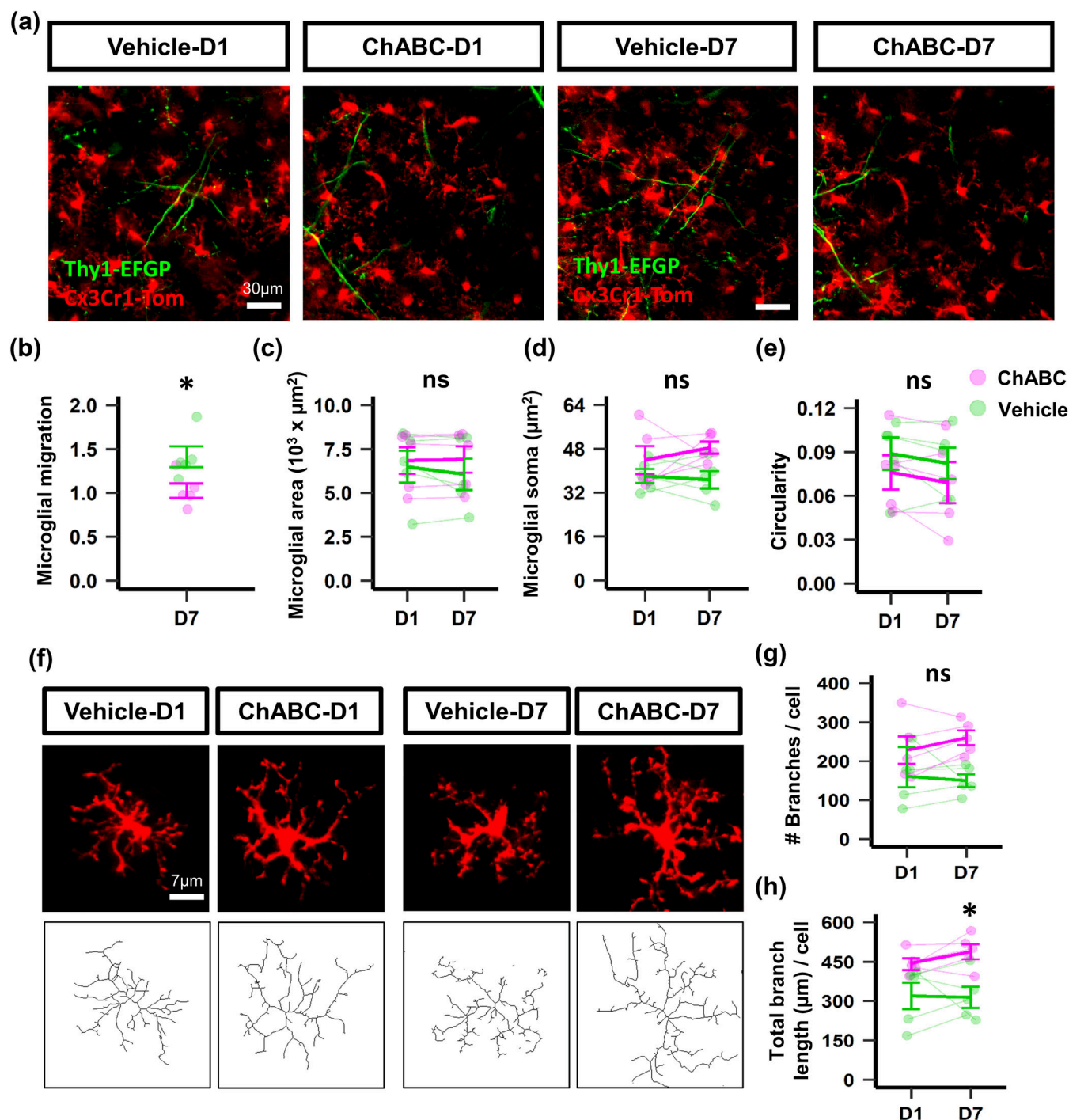
FIGURE 1 Chondroitinase ABC (ChABC) treatment attenuates the expression of neural extracellular matrix (ECM). (a) Experimental design to study the role of ECM in microglia–neuron interactions in the adult brain. Six-week-old Cx3cr1$^{Cre/Tomato}$ × GFPM Thy-1 mice were injected intraperitoneally with tamoxifen for 5 consecutive days to express Tomato in microglia. After 2 months, ChABC, or phosphate-buffered saline were intracerebrally injected into the retrosplenial cortex (RSC) and two-photon imaging sessions were performed after 24 h and 7 days postinjection. (b) Panoramic images of *Wisteria floribunda* agglutinin (WFA) immunostaining in the RSC of ChABC-injected and vehicle group 7 days postinjection (scale bar = 100 μm). (c) Representative images of WFA, aggrecan (Acan), tenascin-R (TN-R), brevican (Bcan), and neurocan (Ncan) immunostainings in ChABC-injected (*n* = 5) and vehicle group (*n* = 5) 7 days postinjection (scale bar = 23 μm). (d, e). Quantitative histological analysis of the ECM. GLM pairwise comparison test: *$p < .05$, **$p < .01$, and ***$p < .001$. Bars and error bars represent mean ± standard error of mean (SEM) values.

(Figure 2c). ChABC treatment did not change the microglial somatic area and circularity compared with the control group at D1 and D7 (Figure 2d,e). However, at D7, microglia from the ChABC group demonstrated more prominently ramified morphology with abundant branched and filamentous cell processes in comparison with the control group (Figure 2e). Branch length was significantly increased in the ChABC group at D7 when compared to the vehicle group

(314.30 ± 40.57 μm vs. 488.53 ± 29.02 μm, $p = .022$) (Figure 2h). The elongated processes and increased branching complexity of microglia could be indicative of a "regulatory" phenotype in response to non-threatening stimuli such as disaccharides and proteins generated from the degradation of CSPGs (Ebert et al., 2008).

To characterize the temporal dynamics of microglial changes due to transient inflammatory response to surgery and injection into the

FIGURE 2 Chondroitinase ABC (ChABC) treatment modifies microglia morphology and migration. (a) Images show microglia population in the retrosplenial cortex in vehicle- and ChABC-treated mice at D1 and D7 postinjection. Microglia are visualized in red and neurons in green (scale bar = 100 μm). (b–e) Plots show microglia recruitment and somatic morphological changes across time and between treatments. Black asterisks indicate differences in the number of microglial cells between vehicle and ChABC groups at D1 and D7, green asterisks denote differences between days for the vehicle group in the generalized estimating equations (GEE) post hoc pairwise comparison with Tukey's test: *p < .05. Line and error bars represent mean ± SEM values. (f) Representative images of morphological changes in microglia branches in vehicle- and ChABC-injected mice. Lower panels show the skeletonized images of microglial cells used for analysis. (g,h) Quantification of the number of branches based on endpoints normalized by the number of microglia cells and total branch length corrected by the number of microglia cells. Black asterisks denote significant differences in the total branch length between vehicle and ChABC treatments at D1 and D7 as detected by the GEE test post hoc pairwise comparison with the Tukey method: *p < .05.

neuropil, microglia were imaged in temporal intervals of over 1, 2, and 3 weeks post cranial window (Figure S2a). Longitudinal imaging of microglial cells in the same mice showed microglial somata to remain stable over the studied time interval. No gross changes in microglial structure were observed (Figure S2b).

3.3 | ChABC treatment modifies microglia interactions with neurons and structural plasticity under basal condition

To explore whether ChABC modifies microglial interactions with synapses, baseline recordings were conducted. For this, 2–3 dendritic branches (48–64 spines) and 3 axonal branches (21–28 axonal boutons) from presumably three different neurons per mouse were followed up for 2 h using two-photon imaging at D1 and D7 postinjection (Figure 3a,b). No differences across time or treatments were found in the area of contact and number of microglia-contacted spines (Figure 3c). The duration of contacts between microglia and dendrites was significantly reduced at D7 (38.97 ± 3.66 min vs. 23 ± 2.13 min, $p = .045$) after ChABC treatment as compared to the vehicle (Figure 3d).

We next examined whether ChABC changes structural synaptic plasticity under basal conditions. Previous studies have proposed that ECM may bidirectionally regulate functional synaptic plasticity. In the present study, analysis of basal turnover of spines, representing their structural plasticity during 2 h on D1 and D7, did not detect any significant effect of ChABC treatment (D1: 2.63% ± 1.44% vs. 2.76% ± 1.69%, $p = 0.999$; D7: 5.09% ± 2.44% vs. 1.48% ± 1.48%, $p = .510$) (Figure 3e). However, compared to the vehicle, ChABC caused a significant increase in spine density at day 7 (Vehicle: 0.987 ± 0.036 vs. ChABC: 1.145 ± 0.03, $p = .014$), mainly due to a decrease in spine elimination rate (Vehicle: 7.159 ± 1.32 vs. ChABC: 0.887 ± 0.34, $p = .003$) (Figure 3f–h). Thus, ECM contributes significantly to the homeostatic mechanisms of synaptic remodeling.

Knowing the effect of ChABC on spine density and microglia-synapse interactions, we wondered whether ChABC treatment would in turn regulate microglia phagocytosis. We found that microglia lysosomal machinery (CD68 expression) was normal (0.98% ± 0.06% vs. 1.11% ± 0.18%, $p = .539$) and detection of synaptic markers in microglia was not changed (1.88% ± 0.22% vs. 3.47% ± 0.75%, $p = .087$) (Figure S3). This suggests that ChABC treatment reduced spine elimination through phagocytosis-independent mechanisms and/or decelerated degradation of endocytosed synaptic markers in microglial lysosomes.

3.4 | ChABC treatment reduces the microglial response towards the synaptic damage

To functionally assess targeted synaptic remodeling by microglia, we introduced a photodamage to an individual spine (Spine-PD) (Figure 3a). After Spine-PD, the contact area of microglia with

dendritic branches was reduced in the ChABC group compared to the vehicle group at D1 (1.94 ± 0.46 μm² vs. 4.02 ± 0.47 μm², $p = .011$) but not at D7 (2.63 ± 0.16 μm² vs. 4.22 ± 0.44 μm², $p = .059$) (Figure 3j). The duration of contact between microglia and spines was shorter after ChABC treatment than in the vehicle group at D7 for Spine-PD (39.29 ± 2.11 min vs. 50.74 ± 1.36 min, $p = .008$) but the number of microglia-contacted spines was not affected by ChABC (Figure 3k,l).

3.5 | Attenuation of neural ECM reduces microglial synaptic remodeling

Strikingly, ChABC treatment appeared to prevent spine elimination and significantly reduced spine turnover at D1 and D7 compared to the vehicle group after Spine-PD (D1: 11.68% ± 1.70% vs. 24.22% ± 1.48%, $p = 0.0004$; D7: 10.68% ± 2.18% vs. 22.29% ± 1.17%, $p = .0008$) (Figure 3m). The formation rate was similar in the ChABC-treated dendrites at D1 and D7 for Spine-PD (Figure 3n). Moreover, the elimination of spines was decreased in the ChABC group compared to the vehicle group at D7 after Spine-PD (6.14% ± 0.95% vs. 13.02% ± 0.82%, $p = .011$) (Figure 3o). These data show that the enzymatic digestion of ECM alters the synaptic remodeling associated with PD and prevents the elimination of spines. Similarly, these results support the idea that ECM removal prevents the elimination of spines by reducing their contact with microglia.

As microglia contact was related to profound changes in spine morphology, we explored the formation of spine head filopodia (SHF). Previously, these structures have been reported as another type of synaptic remodeling in homeostatic and inflammatory conditions. Unexpectedly, no significant differences were found in the formation of SHF in Spine-PD after ChABC treatment (Figure 3p).

To better discriminate the specific effects of microglia-synapse interactions from the effects of photodamage alone, we introduced a photodamage site near imaged dendrites (Near-Spine-PD; Figure 3a). This also resulted in a significant decrease in the duration of microglia–neuron contact (D7: 37.5 ± 1.37 min vs. 50.5 ± 2.73 min, $p = .048$) (Figure 4b) and a reduction in spine remodeling (D1: 6.66% ± 2.06% vs. 17.28% ± 1.53%, $p = .001$; D7: 5.33% ± 0.91% vs. 17.87% ± 1.27%, $p = .0006$) (Figure 4d) and spine loss at D7 (D1: 2.71% ± 0.77% vs. 8.90% ± 2.03%, $p = .018$) after ChABC treatment (Figure 4f). No significant changes in SHFs were detected in ChABC-treated brains as compared to the vehicle controls (Figure 4g).

3.6 | ChABC treatment affects axonal remodeling

Because previous studies have provided evidence of presynaptic remodeling by microglia, we imaged axonal boutons and their interactions with microglia. During baseline recordings, the estimates of contact area, contact duration between microglia and axons, and turnover just tended to be reduced in the ChABC group compared to the vehicle group at D7 (Figure 5a–d).
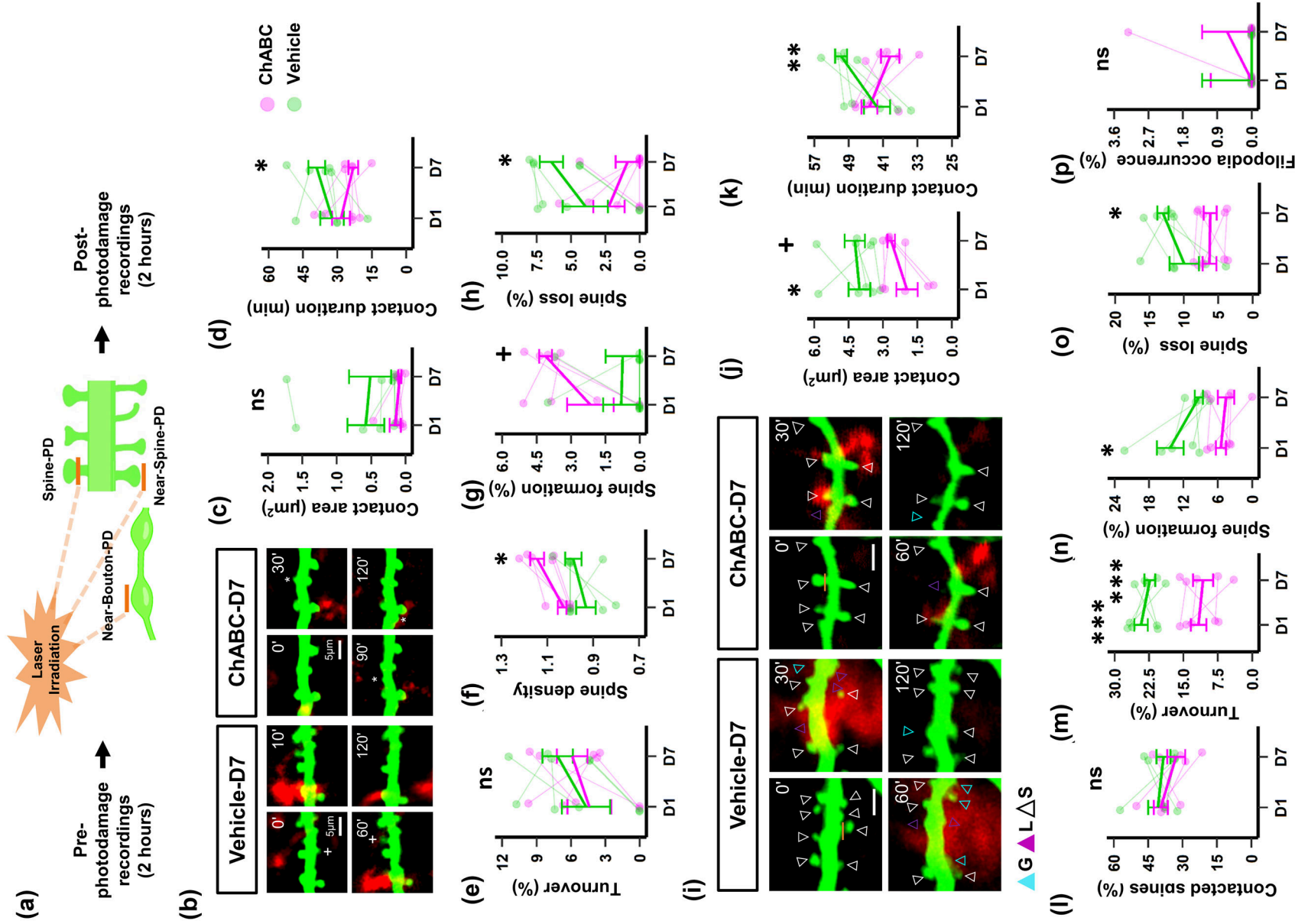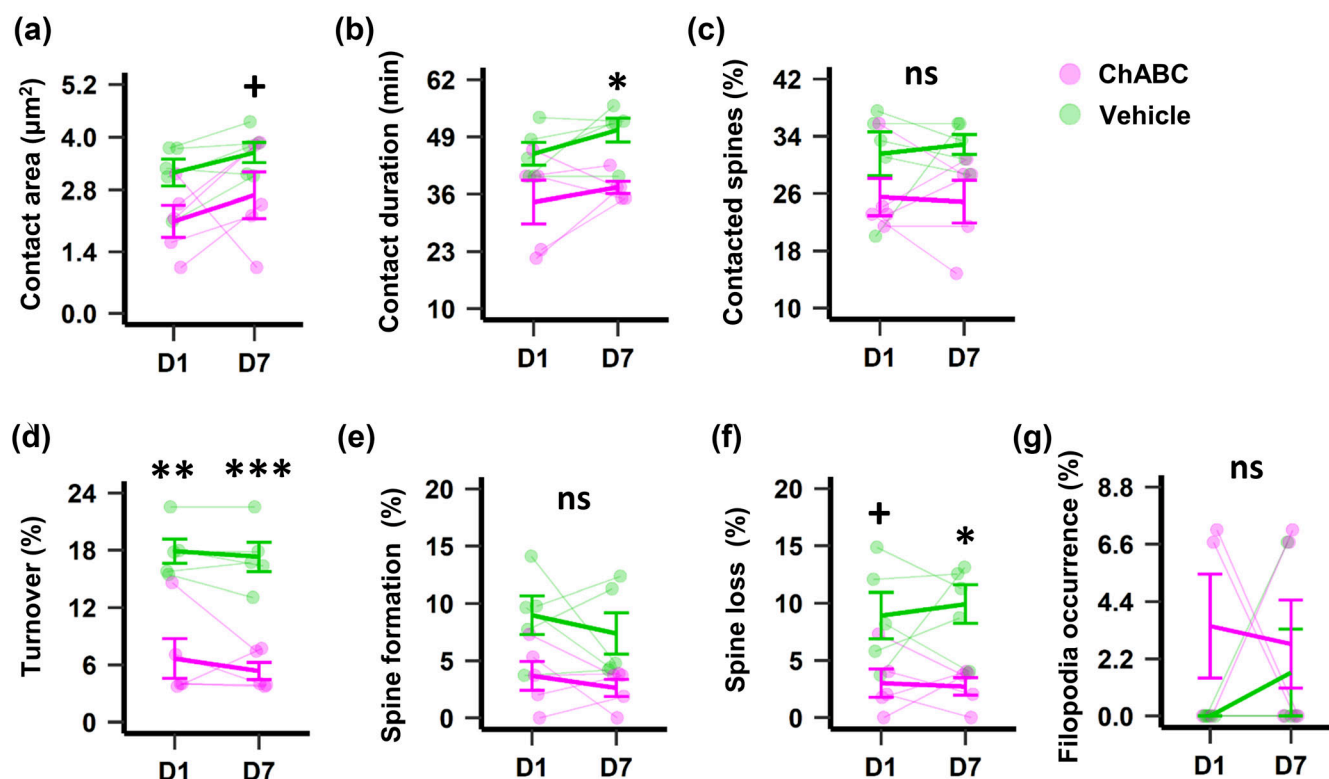
FIGURE 3 Legend on next page.

FIGURE 4 Chondroitinase ABC (ChABC) treatment modifies microglia response towards Near-Spine-photodamage. Time-course of ChABC effects on microglia–neuron interaction parameters after Near-Spine-PD. Black asterisks show multiple comparisons between ChABC ($n = 5$) and vehicle treatments ($n = 5$) at two different times (D1 and D7) for microglia–neuron contact area (a), microglia contact duration with spines/boutons (b), and the number of microglia-contacted spines/boutons (c), synaptic turnover (d), spine formation (e) and loss (f), and filopodia occurrence (g). $^+p = .05$, $^*p < .05$, $^{**}p < .01$, and $^{***}p < .001$ generalized estimating equations test post hoc pairwise multiple comparisons with Tukey's test. Lines and error bars are mean ± SEM.

To functionally assess targeted synaptic remodeling by microglia, we used photodamage to the neuropil near a bouton (Near-Bouton-PD) (Figure 3a). After PD, the contact area of microglia with axonal branches was reduced in the ChABC group compared to the vehicle group at D7 (3.91 ± 0.44 μm² vs. 6.58 ± 0.67 μm², $p = .033$) but not at D1 (Figure 5e). The duration of contact between microglia and boutons and the number of microglia-contacted boutons were not affected by ChABC (Figure 5f,g). Similarly, after Near-Bouton-PD, no

FIGURE 3 Chondroitinase ABC (ChABC) treatment modifies basal and post-photodamage microglia–neuron interactions. (a) Schematic representation of the sessions used to image microglia–neuron interactions pre-photodamage (Baseline) and post-photodamage in the same animal. During each imaging session, three different photodamage experiments (Spine-PD, Near-Spine-PD, and Near-Bouton-PD) were performed using two different dendrites and one axon. In parallel, we selected three adjacent branches, which were recorded simultaneously with the photodamaged branches to obtain the baseline values. Short horizontal bars (≈1 μm) illustrate locations of the photodamaged areas. (b) Baseline recordings of selected dendritic branches were performed every 10 min for 2 h. Time-course of ChABC effects on microglia–neuron interaction parameters at 0, 30, 60, and 120 min. White crosses denote spine elimination and white asterisks show spine formation. (c–h) Comparisons of microglia–neuron contact area and microglia contact duration with spines and spine remodeling between the vehicle ($n = 5$) and ChABC treatments ($n = 5$) at two different times (D1 and D7). Black asterisks denote differences in microglia contact duration between vehicle and ChABC at D1 and D7 as detected by the generalized estimating equations (GEE) test post hoc pairwise comparison with Tukey's method: $^*p < .05$. I. Time-course of ChABC effects on microglia–neuron interaction parameters after Spine-PD. Representative in vivo time-lapse images of interactions (yellow) between microglia (red) and neurons (green) before the PD (0 min) and 30, 60, and 120 min afterward in ChABC- and vehicle-injected mice. Orange lines indicate the laser-targeted position during PD. Stable spines, which remained unchanged over the 2-h imaging period, are indicated by white arrows. Spines that appeared between time points, signifying new growth, are indicated by sky blue arrows. Lost spines that disappeared between time points are indicated by purple arrows (white line = scale bar, 3 μm). (j–p) Black asterisks show multiple comparisons between ChABC ($n = 5$) and vehicle treatments ($n = 5$) at two different times (D1 and D7) for microglia–neuron interaction and synaptic remodeling, $^+p = .05$, $^*p < .05$, $^{**}p < .01$, and $^{***}p < .001$ GEE test post hoc pairwise multiple comparisons with Tukey's test. Lines and error bars are mean ± SEM.
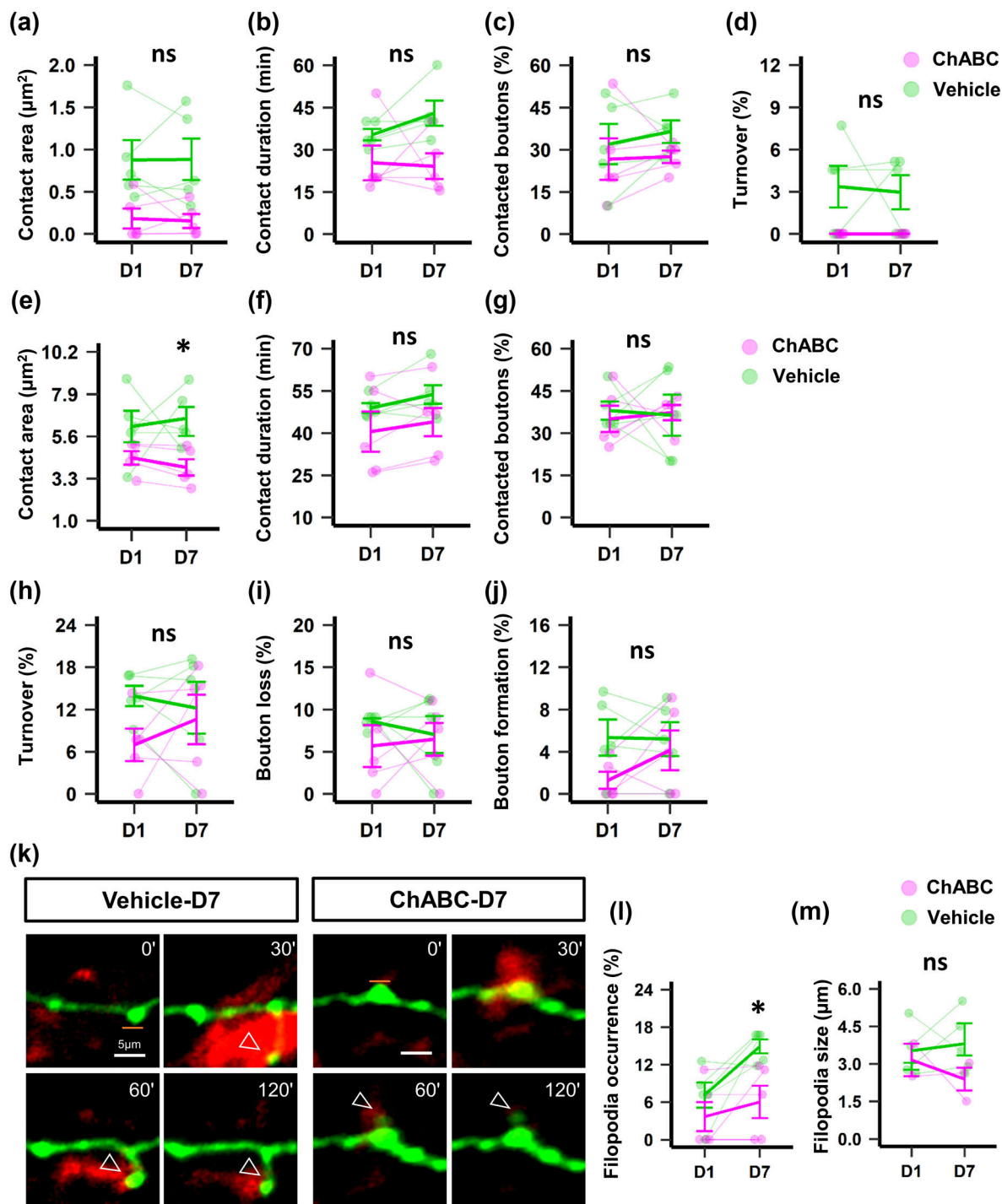
FIGURE 5 Chondroitinase ABC (ChABC) treatment modifies microglia response towards Near-Bouton-photodamage. (a–d) Baseline recordings were performed in selected axonal branches every 10 min for 2 h. Effects of ChABC on microglia contact area (a), duration (b), number of microglia-contacted boutons (c) and turnover (d). Bold lines show group mean ± SEM values, thin lines represent individual animals ($n = 5$ mice per group). *$p < .05$, **$p < .01$, and ***$p < .001$, generalized estimating equations (GEE) post hoc pairwise comparison with Tukey method. (e–j) Results of Near-Bouton photodamage experiments. Black asterisks show multiple comparisons between ChABC ($n = 5$) and vehicle treatments ($n = 5$) at two different times (D1 and D7) for microglia–neuron contact area (e), microglia contact duration with boutons (f), and the number of microglia-contacted boutons (g), synaptic turnover (h), bouton loss (i), and bouton formation (j). $^+p = .05$, *$p < .05$, **$p < 0.01$, and ***$p < .001$ GEE test post hoc pairwise multiple comparisons with Tukey's test. Lines and error bars show mean ± SEM values. (k) Plots show the changes in filopodia occurrence (percentage of replicates per mouse where at least one filopodium was observed after Near-Bouton-PD in ChABC [$n = 5$] and Vehicle [$n = 5$] treated mice. (l, m) Statistical comparisons of filopodia size between vehicle and ChABC: Vehicle-D1, $n = 4$; Vehicle-D7, $n = 5$; ChBAC-D1, $n = 3$; ChABC-D7, $n = 3$. All data points indicate the average value per mouse. Statistical comparisons were performed using GEE test post hoc pairwise comparisons with Tukey's method (*$p < .05$ and ns = not significant).

differences in turnover (%), Gained (%), or Lost (%) boutons were observed between ChABC and control groups on D7 (Figure 5h–j), although on D1 the rates of remodeling and formation of boutons were slightly reduced after ChABC treatment. However, the ChABC treatment affected another form of synaptic remodeling, presynaptic filopodia formation (Figure 5k). The generation of filopodia from boutons was decreased on D7 after ChABC treatment compared with the control group (6.0% ± 2.58% vs., 14.89 ± 1.10%, $p = .039$) (Figure 5l,m). This may be due to short and smaller contacts of microglia with synapses after PD.

3.7 | ChABC treatment impairs expression of complement proteins and dendritic spine tagging

To explore the potential involvement of the complement pathway in the observed reduction of synaptic remodeling following synaptic damage, we focused on C1q, a key mediator in microglia-mediated synaptic remodeling. Compared to the vehicle group, ChABC treatment caused a significant decrease in C1q expression on D1 (Figure S1). Because ChABC treatment induced more pronounced synaptic remodeling in D7 dendrites compared to D1, we assessed the expression of C1q and its binding partner CRT, in D7. Our findings revealed a general decrease in C1q and CRT immunoreactivity at D7 in the ChABC group when compared with the vehicle group (C1q: 1.43 ± 0.32 vs. 12.19 ± 1.06, $p = .0001$; CRT: 4.04 ± 0.49 vs. 6.70 ± 0.47, $p = .008$). Also, expression in microglial cells was reduced (C1q: 0.005 ± 0.001 vs. 0.074 ± 0.020, $p = .013$; CRT: 0.054 ± 0.01 vs. 2.95 ± 1.08, $p = .036$) (Figure 6a,b). Similarly, the expression levels of C3 (0.39 ± 0.18 vs. 1.23 ± 0.23, $p = .028$) and its receptor C3R (1.49 ± 0.24 vs. 4.65 ± 1.15, $p = .036$) were downregulated in the ChABC-treated group at D7 (Figure 6a,b). These findings were not due to direct effect of ChABC on immunostaining of complement proteins because the ChABC treatment of fixed RSC sections ex vivo, which could eliminate WFA staining, did not reduce the intensity of C1q and C3 signals (Figure S4). To determine whether dendritic spines were less susceptible to microglial phagocytosis, we measured the extent of C1q tagging of dendritic spines in both the ChABC-treated and control groups. Notably, the ChABC group exhibited a significantly lower number of C1q-tagged spines compared to the control group (0.02 ± 0.01 vs. 1.49 ± 0.58, $p = .045$) (Figure 6c,d). Further analysis confirmed a reduction in both C1q and CRT, on dendritic spines (10.11 ± 1.71 vs. 29.49 ± 2.87, $p = .001$) (Figure 6c,d). These findings suggest that ChABC treatment compromises normal surveillance of synapses by decreasing the expression of complement proteins, C1q and C3, and the C1q dendritic receptor CRT as well as microglial C3 receptor, CR3. Collectively, these results suggest that the neural ECM plays a crucial role in synaptic remodeling processes carried out by microglia in response to local synaptic damage in a healthy adult brain.

4 | DISCUSSION

Synaptic plasticity regulation by ECM and its influence on microglial functions raised the question of whether the integrity of ECM around synapses modulates synaptic remodeling mediated by microglia. In this study, digestion of ECM led to higher spine density by slowing down spine elimination. Furthermore, impaired spine loss was found to be associated with the reduction in both the duration of microglia-spine contact and the number of synapses tagged with complement proteins. Our findings suggest that ECM integrity is crucial for microglia-dependent structural plasticity and for tissue deposition of eat-me signals.

Here, longer microglial processes were observed after ChABC treatment without effects on microglial soma morphology. This hyper-ramified state of microglia is associated with a noninflammatory state (Maras et al., 2022) and neuroprotective function for microglia (Vinet et al., 2012). This is supported by the evidence that attenuation of ECM by ChABC treatment increases the expression of the anti-inflammatory cytokine IL-10 and reduces the expression of the pro-inflammatory cytokine IL-12B. In line with this, previous studies have shown that disaccharide degradation products of CSPGs after ChABC digestion stimulate microglia to adopt an anti-inflammatory phenotype (Francos-Quijorna et al., 2022) with low cytotoxic potential but high phagocytic activity (Ebert et al., 2008). This activity is presumably aimed at engulfing remaining ECM products as our data show that microglia engulf CSPGs. On the other hand, small soluble degradation products are likely to be removed by clearance mechanisms during the week following ChABC injection.

While an increase in the branching complexity of microglia was observed in ChABC-treated mice, spine density was conserved and the contact duration between microglia and spines was reduced, possibly due to the general effects of neural and perisynaptic ECM loss, changes in the expression of eat-me signals in the extracellular space, and changes in the microglial phenotype. Reduced duration of microglial contacts might influence spine elimination, leading to increased spine density. This aligns with previous studies demonstrating that ChABC treatment strengthens glutamatergic synapses (De Vivo et al., 2013; Orlando et al., 2012). Conversely, longer microglial contact with synapses increases the likelihood of phagocytosis (Cangalaya et al., 2023; Ikegami et al., 2019). Next, the loss of ECM components such as CSPGs (Kirschfink et al., 1997), which have a high affinity for complement proteins, could affect the extracellular accumulation and expression of these proteins. Finally, the observed changes in microglial function may not exclusively result from the attenuation of the neural ECM. As mentioned earlier, degradation products generated by the enzymatic cleavage of chondroitin sulfate side chains by ChABC could exert a direct effect on microglia towards an anti-inflammatory state with an increased debris-clearing activity (Francos-Quijorna et al., 2022). Using synaptic photodamage, we show that synaptic turnover was reduced when the integrity of the ECM was compromised. This could be related to short and less prominent contacts between microglia and synapses after photodamage in the ChABC group, as found in this study. Loss of ECM integrity may contribute to this reduction. This notion is also supported by the fact that enhanced synaptic turnover is associated with prolonged microglia-synapse contact after activation of microglia via lipopolysaccharide or Tau administration (Cangalaya et al., 2023). Since glial presence at synapses is restricted to the extracellular space and depends
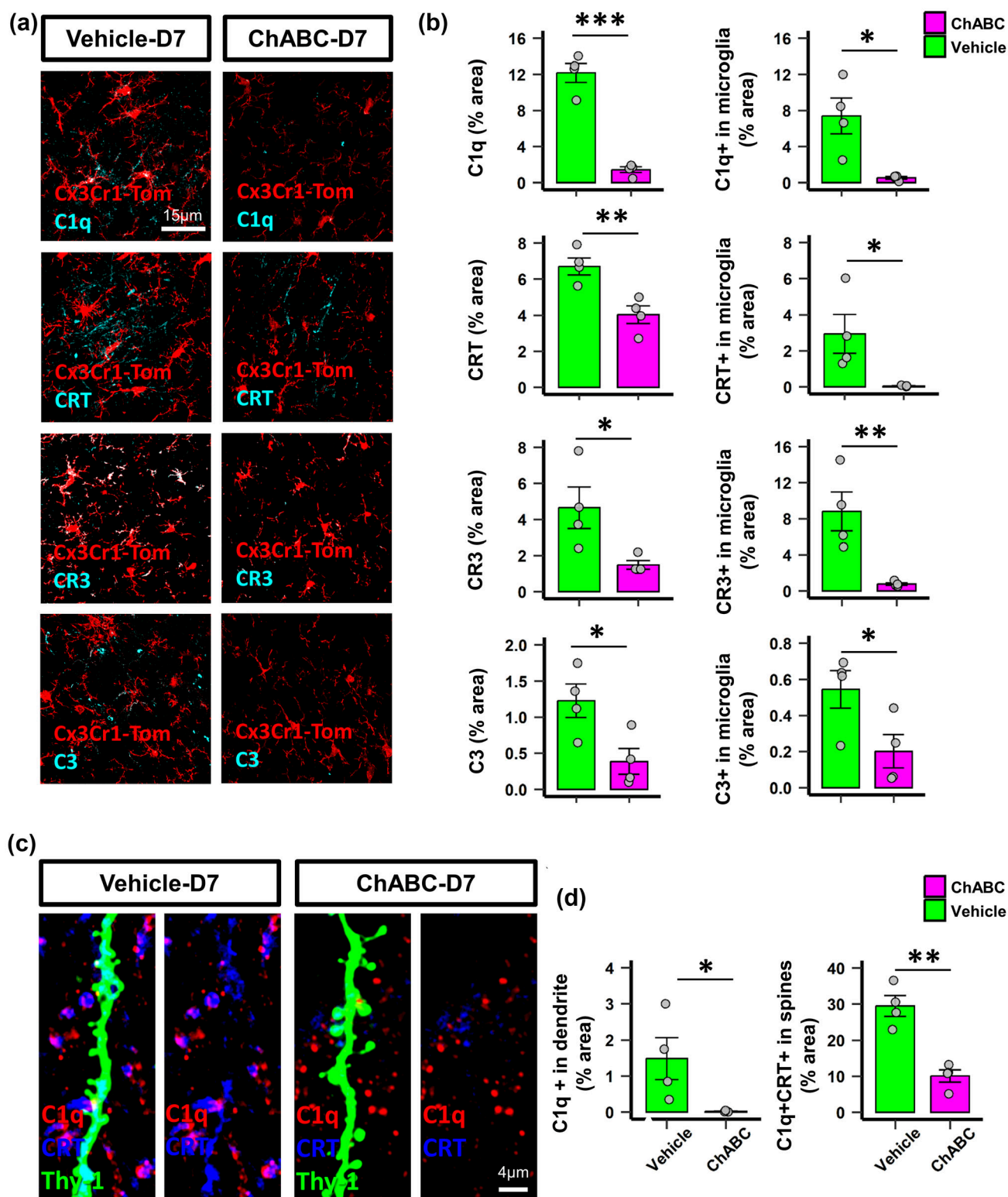
FIGURE 6 Chondroitinase ABC (ChABC) treatment decreases expression of C1q, C3, CR3 and calreticulin (CRT) at synapses. (a) Representative images of C1q, CRT, C3, and C3R expression in ChABC and vehicle groups at D7 (scale bars = 15 μm). (b) Quantification graphs showing changes in the expression of C1q, CRT, C3, and C3R in the retrosplenial cortex and within microglial somata. *$p < .05$, **$p < .01$, and ***$p < .001$, generalized linear model (GLM) pairwise multiple comparisons. Bars and error bars show mean ± SEM values. (c) Representative images of dendritic branches after ChABC treatment at D7, showing the deposition of C1q and its association with calreticulin (CRT) (scale bars = 4 μm). (d) The plots show the quantification of the CA1+ area in dendrites and the area of C1q-CRT colocalization in spines. *$p < .05$ and **$p < .01$, GLM pairwise multiple comparisons. Bars and error bars show mean ± SEM values.

on the matrix geometry (Tremblay et al., 2010), changes in ECM composition and integrity may affect the distribution of microglial processes, therefore, decreasing the contacts between microglia and synapses after photodamage. Because treatment with ChABC is not specific to microglia (Karimi-Abdolrezaee et al., 2012), other cell types might also contribute to the observed reduction in spine elimination. For example, IL-33 expressed by astrocytes can drive microglial synapse engulfment and reduce the numbers of excitatory synapses in the thalamus and spinal cord (Vainchtein et al., 2018). Moreover, loss of neural ECM may affect aggregation of ion channels, postsynaptic receptors, and cell adhesion molecules on neurons, resulting in modulation of inhibitory and excitatory synapses in a cell-autonomous or at least microglia-independent mechanisms (Dzyubenko et al., 2016; Favuzzi et al., 2017; Hayani et al., 2018). Therefore, changes in spine density per se can be interpreted in several ways. Also, the analysis of internalized synaptic markers in microglia reflects synaptic elimination but does not provide an estimate of spine turnover. Thus, the crucial direct evidence that ChABC alters microglia-spine interaction and affects synaptic turnover comes from experiments with synaptic photodamage.

Interestingly, we found that ChABC treatment decreased the protein expression of C1q, C3R, and C3, and very importantly, decreased the number of C1q-tagged spines. These results suggest that neural/ perisynaptic ECM loss may reduce the signals that contribute to synaptic remodeling by microglia. Published data demonstrated that in vivo ChABC-lentivirus administration reduced mRNA expression of C1q and multiple pro-inflammatory genes after spinal cord injury (Francos-Quijorna et al., 2022). Hence, the observed changes in the microglia phenotype and previously reported gene expression changes suggest that altered microglial state is contributing to reduced spine elimination rate after ChABC treatment. Additional mechanism involves changes in (peri)synaptic deposition of complement proteins. This idea supported by the fact that C1q binds directly to CSPGs (Kirschfink et al., 1997; Lopez et al., 2012), which are the target of ChABC. As ChABC treatment leads to a loss of CSPGs and hyaluronan, which otherwise accumulate around synapses, C1q association with spines is also decreased, reducing the likelihood that spines will be phagocytosed by microglia after photodamage. In support of this idea, we also found that ECM attenuation reduces the spine expression of CRT, which is mobilized to the cell surface under endoplasmic reticulum stress and pro-inflammatory conditions and may bind in dendritic spines to C1q (Jeffery et al., 2011). All these changes result in decreased C1q attachment to spines after ChABC treatment and subsequently reduce its recognition by microglia (Figure 7). In addition, intracellular microglial levels of C1q, C3, and C3R were reduced. This is in line with published mRNA expression analysis and single-cell RNA-seq data, which reported elevated C1q and C3R synthesis in pro-inflammatory microglia compared to surveillant microglia (Dejanovic et al., 2022; Liu et al., 2021; Madeshiya et al., 2022; Wu et al., 2023).

Despite the impaired expression of complement system proteins and impaired spine turnover induced by synaptic damage, the basal spine turnover was not changed by ChABC treatment. This is because
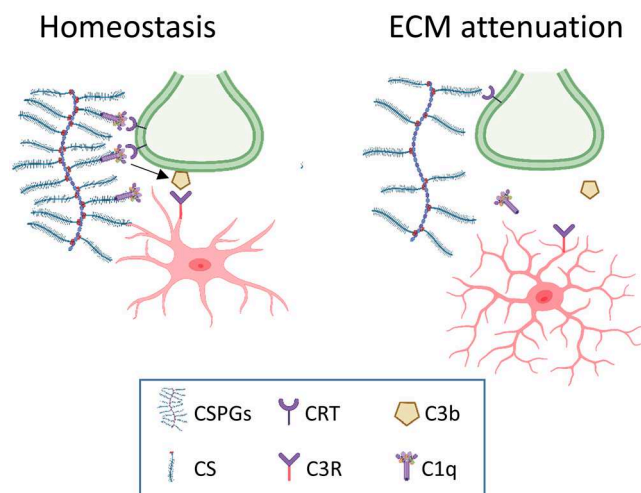
FIGURE 7 A scheme summarizing the role of extracellular matrix (ECM) in synaptic remodeling by microglia. Under normal conditions, synapses are surrounded by perisynaptic ECM enriched in chondroitin sulfate proteoglycans (CSPGs). C1q molecules, which anchor to CSPGs and hyaluronan, can bind directly to synapses or through their dendritic receptor, calreticulin (CRT). The binding of C1q to spines can initiate the tagging of synapses by C3b (marked by arrow). Microglial cells bind C3b through their CR3 receptors and can phagocytose tagged synapses, resulting in selective synapse elimination. When the neuronal ECM is compromised, C1q is not anchored to the CSPGs, the expression levels of C1q and C3 and their receptors, CRT and C3R, are reduced, and spine remodeling is impaired.

the decrease in spine loss was accompanied by elevated spine formation likely due to the major contribution of microglial brain-derived neurotrophic factor (BDNF) and neuronal tropomyosin-related kinase receptor B (TrkB) phosphorylation (Parkhurst et al., 2013). In this context, it is noteworthy that the protein tyrosine phosphatase σ, a receptor for CSPGs, interacts with the BDNF receptor TrkB, and restricts TrkB phosphorylation, while chABC accordingly increases TrkB phosphorylation (Lesnikova et al., 2021). Considering the possibility of BDNF release from microglia and removal of inhibitory constrain for BDNF signaling after ChABC treatment, it is plausible to consider that stimulation of spine formation after ECM attenuation is driven by microglia.

Considering the molecular determinants of ChABC effects on synaptic remodeling by microglia and the complement expression in the brain tissue, it is noteworthy that while ChABC primarily digests chondroitin and dermatan sulfates side chains, it can also break down hyaluronan, releasing proteins bound to these chains directly or indirectly (link proteins, CSPGs such as neurocan) (Deepa et al., 2006; Galtrey et al., 2007; Lin et al., 2008). Consequently, the observed effects on the complement pathway might not solely be due to chondroitin sulfate digestion. They could also involve hyaluronan, particularly as C1q has been shown to avidly bind both high- and low-molecular weight hyaluronan in apoptotic cells (Agostinis et al., 2017; Vidergar et al., 2021).

Besides the extracellular localization of chondroitin sulfate side chains, these molecules may exhibit subcellular localization, being

present for instance on a wide variety of signaling hormones and proteins, including secretogranins (Noborn et al., 2015). CSPGs have been also identified intracellularly in astrocytes and neurons (Aquino et al., 1984; Margolis et al., 1979). On the other hand, ChABC is likely unable to directly penetrate through the cell membrane into cells and act on intracellular chondroitin sulfate-containing proteins. In fact, in vitro studies using brain tissue digestion suggest that about 50% of chondroitin sulfates are accessible to ChABC (Lin et al., 2008), this implies that the rest might be intracellular or could be contained in the stable condensed matrix that is found in perineuronal nets (Deepa et al., 2006). Still, ChABC in complex with CSPGs might be internalized during ECM endocytosis, which occurs at (peri)synaptic sites (Dankovich et al., 2021). Thus, a small amount of intracellular chondroitin sulfates side chains digestion by ChABC might still occur in our experiments and may contribute to the shut-off of synaptic remodeling after ChABC injection.

It is noteworthy that the functional and phenotypic regional heterogeneity of microglia, neurons and the ECM across the brain may yield distinct profiles and drive variable effects of ChABC treatment on synaptic remodeling. The present data support the hypotheses that ECM removal may drive microglia to the anti-inflammatory state and reduce the deposition of local perisynaptic pro-phagocytic cues, which are normally deposited in the ECM. This reinforces the utility of the multipartite synapse concept (Dityatev & Rusakov, 2011), in which the perisynaptic ECM is an essential partner of glial, pre- and postsynaptic specializations. Taken together, these results demonstrate that the critical role of microglia in synaptic remodeling in adult brains depends on the integrity of the neuronal ECM. Hence, our findings highlight a novel role for the ECM and its potential as a therapeutic target for diseases associated with synaptic dysfunction or loss.

AUTHOR CONTRIBUTIONS

ACKNOWLEDGMENTS

FUNDING INFORMATION

CONFLICT OF INTEREST STATEMENT

The authors have declared that no competing interests exist.

DATA AVAILABILITY STATEMENT

The data that support the findings of this study are available from the corresponding author upon reasonable request.

ORCID

Ildiko Rita Dunay https://orcid.org/0000-0002-9900-8605
Alexander Dityatev https://orcid.org/0000-0002-0472-0553

REFERENCES

Agostinis, C., Vidergar, R., Belmonte, B., Mangogna, A., Amadio, L., Geri, P., Borelli, V., Zanconati, F., Tedesco, F., Confalonieri, M., Tripodo, C., Kishore, U., & Bulla, R. (2017). Complement protein C1q binds to hyaluronic acid in the malignant pleural mesothelioma microenvironment and promotes tumor growth. *Frontiers in Immunology*, 8, 1559. https://doi.org/10.3389/fimmu.2017.01559

Aquino, D. A., Margolis, R. U., & Margolis, R. K. (1984). Immunocytochemical localization of a chondroitin sulfate proteoglycan in nervous tissue. II. Studies in developing brain. *The Journal of Cell Biology*, 99(3), 1130–1139. https://doi.org/10.1083/jcb.99.3.1130

Berretta, S., Pantazopoulos, H., Markota, M., Brown, C., & Batzianouli, E. T. (2015). Losing the sugar coating: Potential impact of perineuronal net abnormalities on interneurons in schizophrenia. *Schizophrenia Research*, 167(1–3), 18–27. https://doi.org/10.1016/j.schres.2014.12.040

Bolte, S., & Cordelières, F. P. (2006). A guided tour into subcellular colocalization analysis in light microscopy. *Journal of microscopy*, 224(3), 213–232. https://doi.org/10.1111/j.1365-2818.2006.01706.x

Brückner, G., Bringmann, A., Härtig, W., Köppe, G., Delpech, B., & Brauer, K. (1998). Acute and long-lasting changes in extracellular-matrix chondroitin-sulphate proteoglycans induced by injection of chondroitinase ABC in the adult rat brain. *Experimental Brain Research*, 121(3), 300–310. https://doi.org/10.1007/S002210050463

Cangalaya, C., Stoyanov, S., Fischer, K. D., & Dityatev, A. (2020). Light-induced engagement of microglia to focally remodel synapses in the adult brain. *eLife*, 9, 1–16. https://doi.org/10.7554/ELIFE.58435

Cangalaya, C., Wegmann, S., Sun, W., Diez, L., Gottfried, A., Richter, K., Stoyanov, S., Pakan, J., Fischer, K. D., & Dityatev, A. (2023). Real-time mechanisms of exacerbated synaptic remodeling by microglia in acute models of systemic inflammation and tauopathy. *Brain, Behavior, and Immunity*, 110, 245–259. https://doi.org/10.1016/j.bbi.2023.02.023

Crapser, J. D., Ochaba, J., Soni, N., Reidling, J. C., Thompson, L. M., & Green, K. N. (2020). Microglial depletion prevents extracellular matrix changes and striatal volume reduction in a model of Huntington's disease. *Brain*, 143(1), 266–288. https://doi.org/10.1093/brain/awz363

Crapser, J. D., Spangenberg, E. E., Barahona, R. A., Arreola, M. A., Hohsfield, L. A., & Green, K. N. (2020a). Microglia facilitate loss of perineuronal nets in the Alzheimer's disease brain. *eBioMedicine*, 58, 102919. https://doi.org/10.1016/j.ebiom.2020.102919

Dankovich, T. M., Kaushik, R., Olsthoorn, L. H. M., Petersen, G. C., Giro, P. E., Kluever, V., Agüi-Gonzalez, P., Grewe, K., Bao, G., Beuermann, S., Hadi, H. A., Doeren, J., Klöppner, S., Cooper, B. H., Dityatev, A., & Rizzoli, S. O. (2021). Extracellular matrix remodeling through endocytosis and resurfacing of tenascin-R. *Nature Communications*, 12(1), 1–23. https://doi.org/10.1038/s41467-021-27462-7

De Vivo, L., Landi, S., Panniello, M., Baroncelli, L., Chierzi, S., Mariotti, L., Spolidoro, M., Pizzorusso, T., Maffei, L., & Ratto, G. M. (2013).

Extracellular matrix inhibits structural and functional plasticity of dendritic spines in the adult visual cortex. *Nature Communications*, 4(1), 1–10. https://doi.org/10.1038/ncomms2491

Deepa, S. S., Carulli, D., Galtrey, C., Rhodes, K., Fukuda, J., Mikami, T., Sugahara, K., & Fawcett, J. W. (2006). Composition of perineuronal net extracellular matrix in rat brain: A different disaccharide composition for the net-associated proteoglycans. *Journal of Biological Chemistry*, 281(26), 17789–17800. https://doi.org/10.1074/jbc.M600544200

Dejanovic, B., Wu, T., Tsai, M. C., Graykowski, D., Gandham, V. D., Rose, C. M., Bakalarski, C. E., Ngu, H., Wang, Y., Pandey, S., Rezzonico, M. G., Friedman, B. A., Edmonds, R., De Mazière, A., Rakosi-Schmidt, R., Singh, T., Klumperman, J., Foreman, O., Chang, M. C., ... Hanson, J. E. (2022). Complement C1q-dependent excitatory and inhibitory synapse elimination by astrocytes and microglia in Alzheimer's disease mouse models. *Nature Aging*, 2(9), 837–850. https://doi.org/10.1038/S43587-022-00281-1

Didangelos, A., Iberl, M., Vinsland, E., Bartus, K., & Bradbury, E. J. (2014). Regulation of IL-10 by chondroitinase ABC promotes a distinct immune response following spinal cord injury. *Journal of Neuroscience*, 34(49), 16424–16432. https://doi.org/10.1523/JNEUROSCI.2927-14.2014

Dityatev, A., Frischknecht, R., & Seidenbecher, C. I. (2006). Extracellular matrix and synaptic functions. *Results and Problems in Cell Differentiation*, 43, 69–97. https://doi.org/10.1007/400_025

Dityatev, A., Schachner, M., & Sonderegger, P. (2010). The dual role of the extracellular matrix in synaptic plasticity and homeostasis. *Nature reviews neuroscience*, 11(11), 735–746. https://doi.org/10.1038/nrn2898

Dityatev, A., & Rusakov, D. A. (2011). Molecular signals of plasticity at the tetrapartite synapse. *Current opinion in neurobiology*, 21(2), 353–359. https://doi.org/10.1016/j.conb.2010.12.006

Dityatev, A., & Schachner, M. (2003). Extracellular matrix molecules and synaptic plasticity. *Nature Reviews Neuroscience*, 4(6), 456–468. https://doi.org/10.1038/nrn1115

Dityatev, A., & Schachner, M. (2006). The extracellular matrix and synapses. In *Cell and tissue research* (Vol. 326, 2, pp. 647–654). Springer. https://doi.org/10.1007/s00441-006-0217-1

Dzyubenko, E., Rozenberg, A., Hermann, D. M., & Faissner, A. (2016). Colocalization of synapse marker proteins evaluated by STED-microscopy reveals patterns of neuronal synapse distribution in vitro. *Journal of Neuroscience Methods*, 273, 149–159. https://doi.org/10.1016/J.JNEUMETH.2016.09.001

Ebert, S., Schoeberl, T., Walczak, Y., Stoecker, K., Stempfl, T., Moehle, C., Weber, B. H. F., & Langmann, T. (2008). Chondroitin sulfate disaccharide stimulates microglia to adopt a novel regulatory phenotype. *Journal of Leukocyte Biology*, 84(3), 736–740. https://doi.org/10.1189/JLB.0208138

Faissner, A., Pyka, M., Geissler, M., Sobik, T., Frischknecht, R., Gundelfinger, E. D., & Seidenbecher, C. (2010). Contributions of astrocytes to synapse formation and maturation - potential functions of the perisynaptic extracellular matrix. *Brain research reviews*, 63(1–2), 26–38. https://doi.org/10.1016/j.brainresrev.2010.01.001

Favuzzi, E., Marques-Smith, A., Deogracias, R., Winterflood, C. M., Sánchez-Aguilera, A., Mantoan, L., Maeso, P., Fernandes, C., Ewers, H., & Rico, B. (2017). Activity-dependent gating of parvalbumin interneuron function by the perineuronal net protein brevican. *Neuron*, 95(3), 639–655. https://doi.org/10.1016/j.neuron.2017.06.028

Fawcett, J. W., Oohashi, T., & Pizzorusso, T. (2019). The roles of perineuronal nets and the perinodal extracellular matrix in neuronal function. *Nature reviews neuroscience*, 20(8), 451–465. https://doi.org/10.1038/s41583-019-0196-3

Feng, G., Mellor, R. H., Bernstein, M., Keller-Peck, C., Nguyen, Q. T., Wallace, M., Nerbonne, J. M., Lichtman, J. W., & Sanes, J. R. (2000). Imaging neuronal subsets in transgenic mice expressing multiple spectral variants of GFP. *Neuron*, 28(1), 41–51. https://doi.org/10.1016/S0896-6273(00)00084-2

Francos-Quijorna, I., Sánchez-Petidier, M., Burnside, E. R., Badea, S. R., Torres-Espin, A., Marshall, L., de Winter, F., Verhaagen, J., Moreno-Manzano, V., & Bradbury, E. J. (2022). Chondroitin sulfate proteoglycans prevent immune cell phenotypic conversion and inflammation resolution via TLR4 in rodent models of spinal cord injury. *Nature. Communications*, 13(1), 2933. https://doi.org/10.1038/S41467-022-30467-5

Fung, S., Smith, C. L., Prater, K. E., Case, A., Green, K., Osnis, L., Winston, C., Kinoshita, Y., Sopher, B., Morrison, R. S., Garden, G. A., & Jayadev, S. (2020). Early-onset familial Alzheimer disease variant PSEN2 N141I heterozygosity is associated with altered microglia phenotype. *Journal of Alzheimer's Disease*, 77(2), 675–688. https://doi.org/10.3233/JAD-200492

Galtrey, C. M., Asher, R. A., Nothias, F., & Fawcett, J. W. (2007). Promoting plasticity in the spinal cord with chondroitinase improves functional recovery after peripheral nerve repair. *Brain*, 130(4), 926–939. https://doi.org/10.1093/brain/awl372

Gökçe, O., Bonhoeffer, T., & Scheuss, V. (2016). Clusters of synaptic inputs on dendrites of layer 5 pyramidal cells in mouse visual cortex. *eLife*, 5, e09222. https://doi.org/10.7554/eLife.09222

Hattori, R., Danskin, B., Babic, Z., Mlynaryk, N., & Komiyama, T. (2019). Area-specificity and plasticity of history-dependent value coding during learning. *Cell*, 177(7), 1858–1872. https://doi.org/10.1016/j.cell.2019.04.027

Hayani, H., Song, I., & Dityatev, A. (2018). Increased excitability and reduced excitatory synaptic input into fast-spiking CA2 interneurons after enzymatic attenuation of extracellular matrix. *Frontiers in Cellular Neuroscience*, 12. https://doi.org/10.3389/fncel.2018.00149

Helmut, K., Hanisch, U. K., Noda, M., & Verkhratsky, A. (2011). Physiology of microglia. *Physiological Reviews*, 91(2), 461–553. https://doi.org/10.1152/physrev.00011.2010

Hockfield, S., Kalb, R. G., Zaremba, S., & Fryer, H. (1990). Expression of neural proteoglycans correlates with the acquisition of mature neuronal properties in the mammalian brain. *Cold Spring Harbor Symposia on Quantitative Biology*, 55, 505–514. https://doi.org/10.1101/sqb.1990.055.01.049

Holmes, J. R., & Berkowitz, A. (2014). Dendritic orientation and branching distinguish a class of multifunctional turtle spinal interneurons. *Frontiers in Neural Circuits*, 8, 136. https://doi.org/10.3389/fncir.2014.00136

Holtmaat, A., De Paola, V., Wilbrecht, L., & Knott, G. W. (2008). Imaging of experience-dependent structural plasticity in the mouse neocortex in vivo. *Behavioural Brain Research*, 192(1), 20–25. https://doi.org/10.1016/j.bbr.2008.04.005

Holtmaat, A. J. G. D., Trachtenberg, J. T., Wilbrecht, L., Shepherd, G. M., Zhang, X., Knott, G. W., & Svoboda, K. (2005). Transient and persistent dendritic spines in the neocortex in vivo. *Neuron*, 45(2), 279–291. https://doi.org/10.1016/j.neuron.2005.01.003

Ikegami, A., Haruwaka, K., & Wake, H. (2019). Microglia: Lifelong modulator of neural circuits. *Neuropathology: Official Journal of the Japanese Society of Neuropathology*, 39(3), 173–180. https://doi.org/10.1111/neup.12560

Jeffery, E., Peters, L. R., & Raghavan, M. (2011). The polypeptide binding conformation of calreticulin facilitates its cell-surface expression under conditions of endoplasmic reticulum stress. *The Journal of Biological Chemistry*, 286(4), 2402–2415. https://doi.org/10.1074/JBC.M110.180877

Karimi-Abdolrezaee, S., Schut, D., Wang, J., & Fehlings, M. G. (2012). Chondroitinase and growth factors enhance activation and oligodendrocyte differentiation of endogenous neural precursor cells after spinal cord injury. *PLoS One*, 7(5), e37589. https://doi.org/10.1371/JOURNAL.PONE.0037589

Kaushik, R., Lipachev, N., Matuszko, G., Kochneva, A., Dvoeglazova, A., Becker, A., Paveliev, M., & Dityatev, A. (2021). Fine structure analysis

of perineuronal nets in the ketamine model of schizophrenia. *European Journal of Neuroscience*, 53(12), 3988–4004. https://doi.org/10.1111/ejn.14853

Kettenmann, H., Kirchhoff, F., & Verkhratsky, A. (2013). Microglia: New roles for the synaptic stripper. *Neuron*, 77(1), 10–18. https://doi.org/10.1016/j.neuron.2012.12.023

Kirschfink, M., Blase, L., Engelmann, S., & Schwartz-Albiez, R. (1997). Secreted chondroitin sulfate proteoglycan of human B cell lines binds to the complement protein C1q and inhibits complex formation of C1. *The Journal of Immunology*, 158(3), 1324–1331. https://doi.org/10.4049/jimmunol.158.3.1324

Lenz, K. M., & McCarthy, M. M. (2015). A starring role for microglia in brain sex differences. *Neuroscientist*, 21(3), 306–321. https://doi.org/10.1177/1073858414536468

Lesnikova, A., Casarotto, P. C., Fred, S. M., Voipio, M., Winkel, F., Steinzeig, A., Antila, H., Umemori, J., Biojone, C., & Castrén, E. (2021). Chondroitinase and antidepressants promote plasticity by releasing TRKB from dephosphorylating control of PTPσ in parvalbumin neurons. *The Journal of Neuroscience*, 41(5), 972–980. https://doi.org/10.1523/JNEUROSCI.2228-20.2020

Lian, H., Roy, E., & Zheng, H. (2016). Microglial phagocytosis assay. *Bio-Protocol*, 6(21). https://doi.org/10.21769/BIOPROTOC.1988

Lin, R., Kwok, J. C. F., Crespo, D., & Fawcett, J. W. (2008). Chondroitinase ABC has a long-lasting effect on chondroitin sulphate glycosaminoglycan content in the injured rat brain. *Journal of Neurochemistry*, 104(2), 400–408. https://doi.org/10.1111/J.1471-4159.2007.05066.X

Liu, X., Ma, J., Ding, G., Gong, Q., Wang, Y., Yu, H., & Cheng, X. (2021). Microglia Polarization from M1 toward M2 phenotype is promoted by astragalus polysaccharides mediated through inhibition of miR-155 in experimental autoimmune encephalomyelitis. *Oxidative Medicine and Cellular Longevity*, 2021, 1–15. https://doi.org/10.1155/2021/5753452

Lively, S., & Schlichter, L. C. (2013). The microglial activation state regulates migration and roles of matrix-dissolving enzymes for invasion. *Journal of Neuroinflammation*, 10. https://doi.org/10.1186/1742-2094-10-75

Lopez, M. E., Klein, A. D., & Scott, M. P. (2012). Complement is dispensable for neurodegeneration in Niemann-pick disease type C. *Journal of Neuroinflammation*, 9. https://doi.org/10.1186/1742-2094-9-216

Lupori, L., Totaro, V., Cornuti, S., Ciampi, L., Carrara, F., Grilli, E., Viglione, A., Tozzi, F., Putignano, E., Mazziotti, R., Amato, G., Gennaro, C., Tognini, P., & Pizzorusso, T. (2023). A comprehensive atlas of perineuronal net distribution and colocalization with parvalbumin in the adult mouse brain. *Cell Reports*, 42(7), 112788. https://doi.org/10.1016/j.celrep.2023.112788

Madeshiya, A. K., Whitehead, C., Tripathi, A., & Pillai, A. (2022). C1q deletion exacerbates stress-induced learned helplessness behavior and induces neuroinflammation in mice. *Translational Psychiatry*, 12(1). https://doi.org/10.1038/S41398-022-01794-4

Madisen, L., Zwingman, T. A., Sunkin, S. M., Oh, S. W., Zariwala, H. A., Gu, H., Ng, L. L., Palmiter, R. D., Hawrylycz, M. J., Jones, A. R., Lein, E. S., & Zeng, H. (2010). A robust and high-throughput Cre reporting and characterization system for the whole mouse brain. *Nature Neuroscience*, 13(1), 133–140. https://doi.org/10.1038/nn.2467

Maras, P. M., Hebda-Bauer, E. K., Hagenauer, M. H., Hilde, K. L., Blandino, P., Watson, S. J., & Akil, H. (2022). Differences in microglia morphological profiles reflect divergent emotional temperaments: Insights from a selective breeding model. *Translational Psychiatry*, 12(1), 1–11. https://doi.org/10.1038/s41398-022-01821-4

Margolis, R. K., Thomas, M. D., Crockett, C. P., & Margolis, R. U. (1979). Presence of chondroitin sulfate in the neuronal cytoplasm. *Proceedings of the National Academy of Sciences of the United States of America*, 76(4), 1711–1715. https://doi.org/10.1073/pnas.76.4.1711

Matuszko, G., Curreli, S., Kaushik, R., Becker, A., & Dityatev, A. (2017). Extracellular matrix alterations in the ketamine model of schizophrenia. *Neuroscience*, 350, 13–22. https://doi.org/10.1016/j.neuroscience.2017.03.010

Milner, R., & Campbell, I. L. (2003). The extracellular matrix and cytokines regulate microglial integrin expression and activation. *The Journal of Immunology*, 170(7), 3850–3858. https://doi.org/10.4049/jimmunol.170.7.3850

Morrison, H. W., & Filosa, J. A. (2013). A quantitative spatiotemporal analysis of microglia morphology during ischemic stroke and reperfusion. *Journal of Neuroinflammation*, 10. https://doi.org/10.1186/1742-2094-10-4

Nguyen, P. T., Dorman, L. C., Pan, S., Vainchtein, I. D., Han, R. T., Nakao-Inoue, H., Taloma, S. E., Barron, J. J., Molofsky, A. B., Kheirbek, M. A., & Molofsky, A. V. (2020). Microglial remodeling of the extracellular matrix promotes synapse plasticity. *Cell*, 182(2), 388–403. https://doi.org/10.1016/j.cell.2020.05.050

Nimmerjahn, A., Kirchhoff, F., & Helmchen, F. (2005). Neuroscience: Resting microglial cells are highly dynamic surveillants of brain parenchyma in vivo. *Science*, 308(5726), 1314–1318. https://doi.org/10.1126/science.1110647

Noborn, F., Gomez Toledo, A., Sihlbom, C., Lengqvist, J., Fries, E., Kjellén, L., Nilsson, J., & Larson, G. (2015). Identification of chondroitin sulfate linkage region glycopeptides reveals prohormones as a novel class of proteoglycans. *Molecular & Cellular Proteomics*, 14(1), 41–49. https://doi.org/10.1074/mcp.M114.043703

Orlando, C., Ster, J., Gerber, U., Fawcett, J. W., & Raineteau, O. (2012). Perisynaptic chondroitin sulfate proteoglycans restrict structural plasticity in an integrin-dependent manner. *Journal of Neuroscience*, 32(50), 18009–18017. https://doi.org/10.1523/JNEUROSCI.2406-12.2012

Parkhurst, C. N., Yang, G., Ninan, I., Savas, J. N., Yates, J. R., Lafaille, J. J., Hempstead, B. L., Littman, D. R., & Gan, W. B. (2013). Microglia promote learning-dependent synapse formation through brain-derived neurotrophic factor. *Cell*, 155(7), 1596–1609. https://doi.org/10.1016/j.cell.2013.11.030

Schwartz, N. B., & Domowicz, M. S. (2018). Proteoglycans in brain development and pathogenesis. *FEBS Letters*, 592(23), 3791–3805. https://doi.org/10.1002/1873-3468.13026

Senkov, O., Andjus, P., Radenovic, L., Soriano, E., & Dityatev, A. (2014). Neural ECM molecules in synaptic plasticity, learning, and memory. *Progress in Brain Research*, 214, 53–80. https://doi.org/10.1016/B978-0-444-63486-3.00003-7

Stoyanov, S., Sun, W., Düsedau, H. P., Cangalaya, C., Choi, I., Mirzapourdelavar, H., Baidoe-Ansah, D., Kaushik, R., Neumann, J., Dunay, I. R., & Dityatev, A. (2021). Attenuation of the extracellular matrix restores microglial activity during the early stage of amyloidosis. *Glia*, 69(1), 182–200. https://doi.org/10.1002/glia.23894

Strackeljan, L., Baczynska, E., Cangalaya, C., Baidoe-Ansah, D., Wlodarczyk, J., Kaushik, R., & Dityatev, A. (2021). Microglia depletion-induced remodeling of extracellular matrix and excitatory synapses in the hippocampus of adult mice. *Cells*, 10(8). https://doi.org/10.3390/cells10081862

Tejera, D., Mercan, D., Sanchez-Caro, J. M., Hanan, M., Greenberg, D., Soreq, H., Latz, E., Golenbock, D., & Heneka, M. T. (2019). Systemic inflammation impairs microglial Aβ clearance through NLRP 3 inflammasome. *The EMBO Journal*, 38(17), e101064. https://doi.org/10.15252/embj.2018101064

Thévenaz, P., Ruttimann, U. E., & Unser, M. (1998). A pyramid approach to subpixel registration based on intensity. *IEEE Transactions on Image Processing*, 7(1), 27–41. https://doi.org/10.1109/83.650848

Tremblay, M.-È., Lowery, R. L., & Majewska, A. (2010). Microglial interactions with synapses are modulated by visual experience. *PLoS Biology*, 8(11), e1000527. https://doi.org/10.1371/journal.pbio.1000527

Vainchtein, I. D., Chin, G., Cho, F. S., Kelley, K. W., Miller, J. G., Chien, E. C., Liddelow, S. A., Nguyen, P. T., Nakao-Inoue, H., Dorman, L. C., Akil, O., Joshita, S., Barres, B. A., Paz, J. T.,

Molofsky, A. B., & Molofsky, A. V. (2018). Astrocyte-derived interleukin-33 promotes microglial synapse engulfment and neural circuit development. *Science*, *359*(6381), 1269–1273. https://doi.org/10.1126/SCIENCE.AAL3589

Venturino, A., Schulz, R., De Jesús-Cortés, H., Maes, M. E., Nagy, B., Reilly-Andújar, F., Colombo, G., Cubero, R. J. A., Schoot Uiterkamp, F. E., Bear, M. F., & Siegert, S. (2021). Microglia enable mature perineuronal nets disassembly upon anesthetic ketamine exposure or 60-Hz light entrainment in the healthy brain. *Cell Reports*, *36*(1), 109313. https://doi.org/10.1016/j.celrep.2021.109313

Vidergar, R., Balduit, A., Zacchi, P., Agostinis, C., Mangogna, A., Belmonte, B., Grandolfo, M., Salton, F., Biolo, M., Zanconati, F., Confalonieri, M., & Bulla, R. (2021). C1q-HA matrix regulates the local synthesis of hyaluronan in malignant pleural mesothelioma by modulating HAS3 expression. *Cancers (Basel)*, *13*(3), 416. https://doi.org/10.3390/cancers13030416

Villa, A., Gelosa, P., Castiglioni, L., Cimino, M., Rizzi, N., Pepe, G., Lolli, F., Marcello, E., Sironi, L., Vegeto, E., & Maggi, A. (2018). Sex-specific features of microglia from adult mice. *Cell Reports*, *23*(12), 3501–3511. https://doi.org/10.1016/j.celrep.2018.05.048

Vinet, J., van Weering, H. R. J., Heinrich, A., Kälin, R. E., Wegner, A., Brouwer, N., Heppner, F. L., van Rooijen, N., Boddeke, H. W. G. M., & Biber, K. (2012). Neuroprotective function for ramified microglia in hippocampal excitotoxicity. *Journal of Neuroinflammation*, *9*(1), 1–15. https://doi.org/10.1186/1742-2094-9-27

Wake, H., Moorhouse, A. J., Jinno, S., Kohsaka, S., & Nabekura, J. (2009). Resting microglia directly monitor the functional state of synapses in vivo and determine the fate of ischemic terminals. *Journal of Neuroscience*, *29*(13), 3974–3980. https://doi.org/10.1523/JNEUROSCI.4363-08.2009

Wu, X., Fu, Y., Knott, G., Lu, J., Di Cristo, G., & Josh Huang, Z. (2012). GABA signaling promotes synapse elimination and axon pruning in developing cortical inhibitory interneurons. *Journal of Neuroscience*, *32*(1), 331–343. https://doi.org/10.1523/JNEUROSCI.3189-11.2012

Wu, X., Gao, Y., Shi, C., Tong, J., Ma, D., Shen, J., Yang, J., & Ji, M. (2023). Complement C1q drives microglia-dependent synaptic loss and cognitive impairments in a mouse model of lipopolysaccharide-induced neuroinflammation. *Neuropharmacology*, *237*, 109646. https://doi.org/10.1016/J.NEUROPHARM.2023.109646

Yona, S., Kim, K. W., Wolf, Y., Mildner, A., Varol, D., Breker, M., Strauss-Ayali, D., Viukov, S., Guilliams, M., Misharin, A., Hume, D. A., Perlman, H., Malissen, B., Zelzer, E., & Jung, S. (2013). Fate mapping reveals origins and dynamics of monocytes and tissue macrophages under homeostasis. *Immunity*, *38*(1), 79–91. https://doi.org/10.1016/j.immuni.2012.12.001

Young, K., & Morrison, H. (2018). Quantifying microglia morphology from photomicrographs of immunohistochemistry prepared tissue using ImageJ. *Journal of Visualized Experiments*, *2018*(136). https://doi.org/10.3791/57648

SUPPORTING INFORMATION

Additional supporting information can be found online in the Supporting Information section at the end of this article.